International Journal of Mechanical Sciences 309 (2026) 111010

Contents lists available at ScienceDirect

International Journal of Mechanical Sciences

journal homepage: www.elsevier.com/locate/ijmecsci

Computational modeling of sea ice freezing dynamics across scales

Raghav Pathak [a], Seyed Morteza Seyedpour [a,b,*], Bernd Kutschan [c], Andrea Thom [a], Silke Thoms [c], Tim Ricken [a,b,*]

[a] Institute of Structural Mechanics and Dynamics in Aerospace Engineering, University of Stuttgart, Pfaffenwaldring 27, Stuttgart, 70569, Germany
[b] Porous Media Lab, Institute of Structural Mechanics and Dynamics in Aerospace Engineering, Faculty of Aerospace Engineering and Geodesy, University of Stuttgart, Pfaffenwaldring 27, Stuttgart, 70569, Germany
[c] Ecological Chemistry, Alfred Wegener Institute, Am Handelshafen 12, Bremerhaven, 27570, Germany

ARTICLE INFO

Keywords:
Sea ice
Climate modeling
Computational mechanics
Multiscale phase transition
Extended theory of porous media (eTPM)

ABSTRACT

In recent years, drastic fluctuations in sea ice extent have underscored the critical need to deepen our understanding of its role in the global climate system. Beyond its climatic relevance, variations in sea ice extent and microstructure significantly influence ecological systems, particularly affecting microbial communities like ice algae that inhabit the porous structures within the ice. While large-scale models of sea ice dynamics have seen ongoing development and refinement, the intricate small-scale interactions involving temperature, salinity, and phase change processes remain inadequately captured. This study introduces a comprehensive multiscale modeling framework that captures thermodynamically consistent phase transitions between ocean water and sea ice. At the microscale, a phase-field model is utilized to simulate the formation and evolution of pores in the ice. These microscale pore characteristics are subsequently upscaled and incorporated into a macroscale formulation via the extended Theory of Porous Media (eTPM), enabling the prediction of sea ice growth rates. The framework effectively couples multiple physical fields, phases, and spatial scales, thus bridging microscale ice morphology with macroscale ice behavior. Simulation outcomes highlight the robustness and relevance of the proposed approach for modeling sea ice formation processes.

1. Introduction

Sea ice plays a significant role in global climate dynamics [1]. Due to its reflective nature, sea ice plays an essential role in regulating global temperatures by keeping the polar regions cool [2]. Sea ice behavior, extent, and properties also vary between the Arctic and Antarctic regions. Since the beginning of satellite observations, the Arctic has demonstrated a clear declining trend of around 12% in summer ice extent [3]. In contrast, in the last decade, Antarctic sea ice cover has seen unprecedented annual fluctuations, with the highest ice cover recorded in 2014 [4] to a record low in 2023 [5]. These large fluctuations are due to unpredictably varying seasonal temperatures and environmental conditions, suggesting a possible role of climate change in future sea ice concentrations [6,7].

The sea ice is a highly complex porous material with a solid ice matrix filled by liquid interstitial brine inclusions. The brine inclusions serve as habitat for microbial communities, hence, regulating the Southern Ocean biological ecosystem [8]. While quite a fair bit of research infrastructure has been deployed towards understanding large-scale growth and decaying behavior of sea ice, there still lies a huge knowledge gap in both understanding and agreement among academics towards small-scale processes like freezing and thawing.

The physical and mechanical properties of sea ice are a result of several small scale processes associated with temperature and salinity [9,10]. Ice crystals start forming on seawater as thermodynamic consequences of low temperature conditions. The process of phase transition separates ice and brine by releasing salt into adjacent pores. The concentrated brine inside the pores has a higher salinity than the bulk ocean [11]. These complex interactions and processes can be simulated using mathematical models and numerical schemes like Finite Elements [12]. These simulations provide comprehensive insights about the mechanisms that govern these complex physical, and often inaccessible processes.

There have been several attempts to model the growth processes in sea ice. The first discussions were initiated on the evolution of vertical salinity profiles and their effects on the thermal properties of ice [13]. The correlation between mechanical, thermal, and electrical properties of sea ice and brine volume have also been investigated [10]. Equations for determining the brine volume and salinity based on temperature

* Corresponding authors.
E-mail addresses: seyed-morteza.seyedpour@isd.uni-stuttgart.de (S.M. Seyedpour), tim.ricken@isd.uni-stuttgart.de (T. Ricken).

https://doi.org/10.1016/j.ijmecsci.2025.111010
Received 2 July 2025; Received in revised form 28 October 2025; Accepted 9 November 2025
Available online 21 November 2025

have been developed [14]. Description of composite salinity profiles based on third-degree polynomial functions depending on temperature have been computed, providing insights into brine dynamics during various seasons [15]. More comprehensive descriptions of the multiphase materials using the so-called "mushy layer" theory have also been introduced, primarily in the context of metallurgy [16–18]. In the context of sea ice, insights into the desalination mechanisms using the mushy layer theory have been presented in [19]. While it has its own limitations, such as lack of pore scale information and the assumption of homogeneous columnar sea ice growth, mushy layer theory continues to be the most popular approach for modeling freezing and growth related processes in popular sea ice modules like ICEPACK [20] in Community Ice CodE (CICE) [21], and Sea Ice modeling Integrated Initiative (SI^3) [22]. Phase field models of the solid–liquid phase transition of sea ice growth have also been studied [23]. Combined experimental and numerical studies have also led to reliable models of sea ice freezing and heat transfer [24,25].

Recently, advances have also been made in modeling sea ice mechanics across scales [26,27]. Particle and continuum based combined multiscale approaches have also been developed to model sea ice floe behavior [28]. In the context of Arctic sea ice variability prediction, a multiscale approach focused on different time scales has also been developed [29]. Ice Graph Attention neTwork (IceGAT) [30] is a novel neural network model trained to predict sea ice concentration based on multiple spatial resolutions and combining them with physical conservation laws. Multiscale deep learning based models have also been developed to resolve sub seasonal spatiotemporal behaviors of Arctic sea ice [31]. The lightweight prediction approach employs an encoder–decoder structure to predict daily sea ice concentration (SIC) and sea ice thickness (SIT). Such developments have greatly pointed out the importance of approaching sea ice growth and freezing dynamics as a scientific challenge occurring at various resolutions of space and time. While these approaches have certainly enriched the broader scientific literature on multiscale modeling of sea ice properties, certain problems still exist. Uncertainties in data based approaches like machine learning, model complexity and transfer to global large scale models, and extreme variations in the sea ice regions themselves in the north and south poles are just a few of the challenges. While continuum based models pose the challenge of computational cost, they certainly play an effective role in performing fundamental analyses to understand fundamental behaviors and patterns. Further development of these methods have the potential to pave way for improved understanding of sea ice regions, and consequently, prediction of climate events, trends and extremes. The exact multiscale thermodynamic processes involving phase separation due to microscale morphological pattern formation and temperature gradients on the macroscale have not been well understood. Therefore, it becomes natural to model the multiphasic characteristics of sea ice using thermodynamically consistent continuum mechanical theories. A comprehensive formulation for the governing equations of two-phase saturated porous media has been devised [32,33]. Continuum mechanical models for porous materials have been derived using the homogenization approach and mixture theories developed in [34]. Conservation laws for mass, momentum, and energy have been included in these theories. The models have typically been obtained by applying Mixture Theory (MT) [35–37], the Theory of Porous Media (TPM) [38–43], and local volume averaging theory [44–46]. The primary distinctions among the models reside in the theoretical motivations and the manner in which homogenized quantities have been incorporated.

A framework for the multiphase description of complex porous media has been provided by the Theory of Porous Media. It has also been found suitable for modeling phase transition phenomena in porous media [47,48]. An extension of the Theory of Porous Media (eTPM), which allows for a further description of miscible solute components in immiscible phases, has also been introduced [49–51]. In the context of freezing, the suitability of TPM for such problems has also been introduced and well established [52–59]. However, these models have been applied in other contexts of freezing and often lack in resolving one or more fundamental processes, behaviors or constituents pertaining to the sea ice system. The initial TPM models focused on the formation of pure, salt free ice and modeling of frost damage due to volume expansion in civil structures through ternary [54], and quadruple phase models [52], as well as freeze-thaw loads [53]. Various descriptions of ice growth have also been developed. While the equations have been thermodynamically consistent and physically motivated, the physical applicability of growth terms was often restricted by pre-factors and constants required for model calibration, cf. [55]. Further, divergence of heat flux-based growth terms pose computational challenges as well due to spatial gradients and sensitivity to mesh, material, and nonlinearities in the system. Models developed in the context of sea ice have proven to be more sophisticated and to be able to capture several quantities of interest. However, the problem of prefactors persists even with enthalpy-focused ice growth term, cf. [58]. In some cases, sea ice has been investigated as an inhomogeneous material with discontinuous approximation for volume fraction ice [60], the description of the liquid phase often lacks consideration of salt. More recent TPM-based models, such as [61–63], focus on multiphase ice and seawater systems and coupled sea ice physics and biogeochemistry that resolve photosynthesis and carbon assimilation dynamics. This indicates, that further development of TPM based models, specifically developed for sea ice freezing with multiple scales that do not depend on numerical adjustments can be a step in the right direction.

In the context of pattern formation on the microscale, a phase field approach to model pattern formation during the super cooling solidification of a pure material has been presented in [64]. A coupled order parameter and salinity based phase field solidification model to describe brine channel formation in sea ice was been proposed [65]. A Turing model-based approach for brine channel formation has also been presented [66]. This approach has been further modified into a phase field method [65,67]. A model describing the influence of antifreeze proteins on ice growth has been introduced [68]. Anisotropic single crystal growth and directional competitive crystallization behavior has also been modeled in three dimensions recently [69]. Multi-physical coupled phase field and lattice Boltzmann method (LBM) [70] or computational fluid dynamics (CFD) [71] techniques have proven to improve model accuracy by up to 70%. In summary, the phase field approach has been found useful for modeling pattern formation and for determining the size of brine channels and pores in sea ice. An approach to model multiscale micro-macro phase transitions in the context of steel solidification using the phase field on the microscale and TPM on the macroscale has also been proposed in [72].

This paper presents a framework for describing freezing process in new sea ice incorporating multiple scales, phases, and fields. The macroscale freezing behavior is determined to be a consequence of microscale phase separation between ice and liquid brine phases. Both micro and macroscale behavior follows from volumetric coupling of field quantities. The outline of the paper is as follows. First, a multiphase and multicomponent description of the sea ice is presented in the context of continuum mechanics of multiphase mixtures, approached through the Theory of Porous Media (TPM). Next, the considerations and formulations for the phase transition phenomena are discussed in detail on both micro and macroscale. The numerical treatment is then presented on both scales. Finally, academic results are shown and discussed in detail, followed by conclusions and future directions.

2. Material and methods

In this section, the theoretical and numerical framework that forms the multiscale model of sea ice formation is detailed. Starting with Section 2.1, the macroscale physics are established through the introduction of the Extended Theory of Porous Media (eTPM) as the

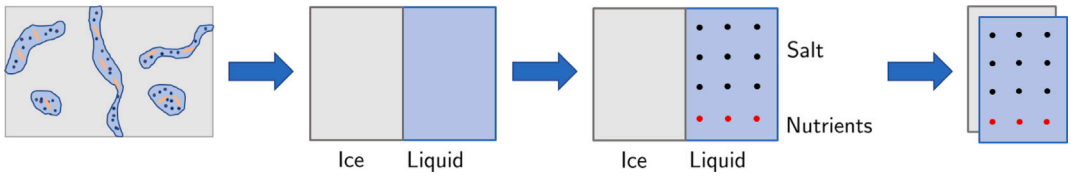

Fig. 1. Homogenization from true to smeared structure with phases.

foundation for describing sea ice as a biphasic material with miscible components in Section 2.2. From this foundation, the governing balance laws, field equations, and crucial constitutive relations for the bulk material are derived in Section 2.3. The macroscale model description is concluded in Section 2.4 with the numerical treatment, in which the weak formulations and the application of the Finite Element Method for solving the fully coupled system of equations are outlined. Following the macroscale formulation, the focus is shifted to the microscale in Section 2.5, where a phase-field solidification model is developed to simulate the intricate dynamics of brine channel and pore formation. In Section 2.6, the micro-macro coupling scheme is then detailed, explaining how microscale pore geometry is calculated and passed back to the macroscale to influence the overall ice growth rate.

2.1. Extended Theory of Porous Media (eTPM)

The foundational principles of the Theory of Porous Media (TPM) stem from the combination of mixture theory and the concept of volume fractions. These principles enable the local composition of a complex aggregate to be systematically described. The extended Theory of Porous Media (eTPM) [73–75] introduces a framework for treating miscible substances φ^β distributed within immiscible macro-phases φ^α. The mixture body φ comprises κ macroscopic phases indexed by $\alpha = 1, \dots, \kappa$. Each immiscible phase may further contain ν miscible components $\varphi^{\alpha\beta}$ transported within φ^α. The composition of the medium is given in Eq. (1), and homogenization yields

$$\varphi = \bigcup_{\alpha}^{\kappa} \varphi^\alpha := \bigcup_{\alpha}^{\kappa} \left(\bigcup_{\beta}^{\nu} \varphi^{\alpha\beta} \right). \tag{1}$$

Sea ice can be modeled as a biphasic system, comprising the solid ice matrix $\varphi^{\mathbf{I}}$ and the liquid brine $\varphi^{\mathbf{L}}$, i.e., $\alpha = \mathbf{I}, \mathbf{L}$. The liquid brine phase $\varphi^{\mathbf{L}}$ contains miscible constituents $\varphi^{\mathbf{L}\beta}$ such as salt (s) and freshwater (w).

Using volume averaging, the distinct phases are uniformly distributed throughout the domain. Fig. 1 illustrates the conceptual transition from the heterogeneous true structure to a homogenized representation involving immiscible and miscible phase decomposition.

The volume fraction n^α is defined in Eq. (2) as the ratio of the partial volume dv^α of the constituent φ^α to the total volume dv:

$$\mathrm{n}^\alpha = \frac{\mathrm{dv}^\alpha}{\mathrm{dv}}. \tag{2}$$

Imposing the constraint that the volume is fully saturated by phases (i.e., no voids), the saturation condition becomes

$$\sum_{\alpha} \mathrm{n}^\alpha = \mathrm{n}^{\mathbf{I}} + \mathrm{n}^{\mathbf{L}} = 1. \tag{3}$$

Given the mass m^α of a constituent, the real and partial densities are defined in Eq. (4):

$$\rho^{\alpha\mathrm{R}} = \frac{\mathrm{dm}^\alpha}{\mathrm{dv}^\alpha}, \quad \text{and} \quad \rho^\alpha = \frac{\mathrm{dm}^\alpha}{\mathrm{dv}}. \tag{4}$$

The relation between these densities via volume fraction is

$$\rho^\alpha = \mathrm{n}^\alpha \, \rho^{\alpha\mathrm{R}}. \tag{5}$$

The real density $\rho^{\alpha\mathrm{R}}$ can be written as the sum of real densities of the miscible components: $\rho^{\alpha\mathrm{R}} = \sum_\beta \rho^{\alpha\beta}$. Consequently, the partial pore densities are given by $\rho^\beta = \mathrm{n}^\alpha \rho^{\alpha\beta}$. Specifically, for the brine liquid containing freshwater and salt:

$$\rho^\beta = \frac{\mathrm{dm}^\beta}{\mathrm{dv}} = \mathrm{n}^{\mathbf{L}} \rho^{\mathbf{L}\beta}, \quad \text{with} \quad \rho^{\mathbf{LR}} = \sum_\beta \rho^{\mathbf{L}\beta} \tag{6}$$

The corresponding mass fraction is the ratio of the local mass of the solute to the total local solute mass: $\mathrm{w}^{\mathbf{L}\beta} = \frac{\rho^{\mathbf{L}\beta}}{\rho^{\mathbf{LR}}}$. To deal with the kinematic relations, each phase is provided with its individual motion functions and their derivatives as shown in Fig. 2. More details on the kinematics are provided in Appendix A.1.

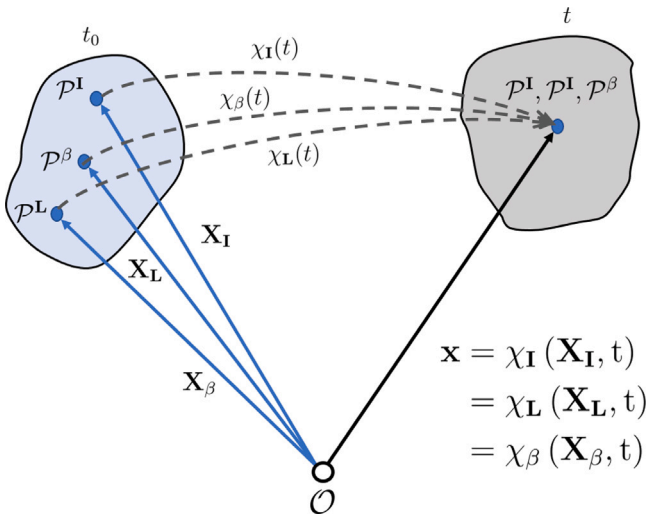

Fig. 2. Kinematics in the framework of TPM.

2.2. Modeling sea ice as a biphasic material with miscible components

To model sea ice as a biphasic material, we apply the extended Theory of Porous Media (eTPM), leveraging Truesdell's metaphysical principles [76]. These principles establish that each constituent, both immiscible phases and miscible components, obeys balance equations analogous to those in classical continuum mechanics. The mass balance for each macroscopic phase φ^α is described by

$$\left(\rho^\alpha\right)'_\alpha + \rho^\alpha \operatorname{div} \mathbf{x}'_\alpha = \hat{\rho}^\alpha, \tag{7}$$

where ρ^α is the partial density, $\mathbf{x}'_\alpha$ is the velocity of phase α, and $\hat{\rho}^\alpha$ represents the mass transfer rate into or out of the phase. Similarly, each miscible component φ^β satisfies

$$\left(\rho^\beta\right)'_\beta + \rho^\beta \operatorname{div} \mathbf{x}'_\beta = \hat{\rho}^\beta, \tag{8}$$

with analogous meaning for the terms, specific to component β. The momentum balance for a macroscopic phase is given by

$$\operatorname{div} \mathbf{T}^\alpha + \rho^\alpha \left(\mathbf{b} - \mathbf{x}''_\alpha\right) = \hat{\rho}^\alpha \mathbf{x}'_\alpha - \hat{\mathbf{p}}^\alpha, \tag{9}$$

where $\mathbf{T}^\alpha$ is the Cauchy stress tensor, $\mathbf{b}$ the body force (typically gravity), and $\hat{\mathbf{p}}^\alpha$ the rate of linear momentum exchange with other constituents. The left-hand side represents internal and external mechanical effects, while the right-hand side includes the contributions from

mass and momentum exchange. Each miscible component similarly satisfies its own momentum balance

$$\operatorname{div}\mathbf{T}^{\beta}+\rho^{\beta}\left(\mathbf{b}-\mathbf{x}_{\beta}''\right)=\hat{\rho}^{\beta}\mathbf{x}_{\beta}'-\hat{\mathbf{p}}^{\beta}. \tag{10}$$

The balance of angular momentum enforces the symmetry of the stress tensor

$$\mathbf{T}^{\alpha}=\left(\mathbf{T}^{\alpha}\right)^{\mathrm{T}}. \tag{11}$$

Energy conservation for a phase is described by the following equation

$$\hat{\rho}^{\alpha}\left(\varepsilon^{\alpha}\right)_{\alpha}'-\mathbf{T}^{\alpha}\cdot\mathbf{D}_{\alpha}-\rho^{\alpha}r^{\alpha}+\operatorname{div}\mathbf{q}^{\alpha}=\hat{e}^{\alpha}-\hat{\mathbf{p}}^{\alpha}\cdot\mathbf{x}_{\alpha}'-\hat{\rho}^{\alpha}\left(\varepsilon^{\alpha}-\frac{1}{2}\mathbf{x}_{\alpha}'\cdot\mathbf{x}_{\alpha}'\right), \tag{12}$$

where ε^{α} is the internal energy, $\mathbf{D}_{\alpha}$ the symmetric part of the velocity gradient, r^{α} the heat supply, $\mathbf{q}^{\alpha}$ the heat flux, and $\hat{e}^{\alpha}$ the energy exchange with other constituents. The last two terms on the right capture mechanical work and kinetic energy exchanges. For each component β, a similar energy equation holds

$$\hat{\rho}^{\beta}\left(\varepsilon^{\beta}\right)_{\beta}'-\mathbf{T}^{\beta}\cdot\mathbf{D}_{\beta}-\rho^{\beta}r^{\beta}+\operatorname{div}\mathbf{q}^{\beta}=\hat{e}^{\beta}-\hat{\mathbf{p}}^{\beta}\cdot\mathbf{x}_{\beta}'-\hat{\rho}^{\beta}\left(\varepsilon^{\beta}-\frac{1}{2}\mathbf{x}_{\beta}'\cdot\mathbf{x}_{\beta}'\right). \tag{13}$$

To ensure that the overall mixture conserves mass, momentum, and energy, the sum of all supply terms across phases must vanish

$$\sum_{\alpha}\hat{\rho}^{\alpha}=0,\quad\sum_{\alpha}\hat{\mathbf{p}}^{\alpha}=\mathbf{0},\quad\sum_{\alpha}\hat{e}^{\alpha}=0. \tag{14}$$

These constraints, known as Truesdell's conditions, are critical for consistency within the eTPM framework and ensure that the mixture as a whole obeys the classical conservation laws.

2.3. Assumptions and field equations

In the present biphasic sea ice model, isothermal conditions are assumed, implying equal temperature $\theta=\theta^{\alpha}$ in all phases. Consequently, the inter-phase energy supply vanishes, i.e., $\hat{e}^{\alpha}=0$. The solid ice matrix is considered incompressible, yet a dependence of its real density on temperature is retained, such that $\rho^{\mathbf{IR}}=\rho^{\mathbf{IR}}(\theta)$. For the brine phase, incompressibility is likewise assumed, while its real density is treated as a function of salinity S^{br}, written as $\rho^{\mathbf{LR}}=\rho^{\mathbf{LR}}(S^{\mathrm{br}})$.

The mass balance for the ice phase and the brine liquid under these assumptions takes the form

$$\begin{aligned}&\left(\mathrm{n}^{\mathbf{I}}\right)_{\mathbf{I}}'\rho^{\mathbf{IR}}+\mathrm{n}^{\mathbf{I}}\left(\rho^{\mathbf{IR}}\right)_{\mathbf{I}}'\operatorname{div}\mathbf{x}_{\mathbf{I}}'=\hat{\rho}^{\mathbf{I}},\\&\left(\mathrm{n}^{\mathbf{L}}\right)_{\mathbf{L}}'\rho^{\mathbf{LR}}+\mathrm{n}^{\mathbf{L}}\left(\rho^{\mathbf{LR}}\right)_{\mathbf{L}}'\operatorname{div}\mathbf{x}_{\mathbf{L}}'=-\hat{\rho}^{\mathbf{I}}.\end{aligned} \tag{15}$$

The time derivatives in the liquid phase are related to those in the solid skeleton frame through a transformation that accounts for the convective contribution from the seepage velocity $\mathbf{w}_{\mathbf{LI}}$. Given a scalar field Γ, the material derivative transforms as

$$(\Gamma)_{\mathbf{L}}'=(\Gamma)_{\mathbf{I}}'+\operatorname{grad}\Gamma\cdot\mathbf{w}_{\mathbf{LI}}. \tag{16}$$

By applying the transformation (16) to the salt density $\rho^{\mathbf{L}\beta}$ and inserting the result into the salt mass conservation law, the following expression is obtained

$$\mathrm{n}^{\mathbf{L}}\left(\rho^{\mathbf{L}\beta}\right)_{\mathbf{I}}'+\left(\mathrm{n}^{\mathbf{L}}\right)_{\mathbf{I}}'\rho^{\mathbf{L}\beta}+\operatorname{div}^{\mathbf{L}}\rho^{\mathbf{L}\beta}\mathbf{w}_{\beta\mathbf{I}}+\mathrm{n}^{\mathbf{L}}\rho^{\mathbf{L}\beta}\operatorname{div}\mathbf{x}_{\mathbf{I}}'=0. \tag{17}$$

Assuming quasi-static conditions, the acceleration terms $\mathbf{x}_{\alpha}''$ vanish. The momentum balances for the ice and brine phases are then given by

$$\operatorname{div}\mathbf{T}^{\mathbf{I}}+\rho^{\mathbf{I}}\mathbf{b}=\hat{\rho}^{\mathbf{I}}\mathbf{x}_{\mathbf{I}}'-\hat{\mathbf{p}}^{\mathbf{I}},\quad\operatorname{div}\mathbf{T}^{\mathbf{L}}+\rho^{\mathbf{L}}\mathbf{b}=-\hat{\rho}^{\mathbf{I}}\mathbf{x}_{\mathbf{L}}'+\hat{\mathbf{p}}^{\mathbf{I}}. \tag{18}$$

Since the total momentum production across all phases must vanish as per Eq. (14), substitution of Eq. (A.5) into Eq. (18) yields the combined momentum balance for the mixture

$$\operatorname{div}\mathbf{T}+\rho\mathbf{b}=-\hat{\rho}^{\mathbf{I}}\mathbf{w}_{\mathbf{LI}}, \tag{19}$$

with $\mathbf{T}=\mathbf{T}^{\mathbf{I}}+\mathbf{T}^{\mathbf{L}}$ and $\rho=\rho^{\mathbf{I}}+\rho^{\mathbf{L}}$ denoting total stress and mixture density.

The energy balance for the mixture, written using the Helmholtz free energy $\psi^{\alpha}=\varepsilon^{\alpha}-\theta^{\alpha}\eta^{\alpha}$, is expressed as

$$\begin{aligned}&\sum_{\alpha}\left\{\rho^{\alpha}\left[\left(\psi^{\alpha}\right)_{\alpha}'+(\theta)_{\alpha}'\eta^{\alpha}+\theta\left(\eta^{\alpha}\right)_{\alpha}'\right]-\mathbf{T}^{\alpha}\cdot\mathbf{D}_{\alpha}\right\}+\operatorname{div}\mathbf{q}\\&=-\hat{\mathbf{p}}^{\mathbf{L}}\cdot\mathbf{w}_{\mathbf{LI}}-\hat{\rho}^{\mathbf{I}}\left(\psi^{\mathbf{I}}-\psi^{\mathbf{L}}+\theta(\eta^{\mathbf{I}}-\eta^{\mathbf{L}})\right),\end{aligned} \tag{20}$$

with total heat flux $\mathbf{q}=\mathbf{q}^{\mathbf{I}}+\mathbf{q}^{\mathbf{L}}$ and specific entropies defined over space and time $\eta^{\alpha}=\eta^{\alpha}(\mathbf{x},\mathbf{t})$. The relations between the brine phase $\varphi^{\mathbf{L}}$ and its components $\varphi^{\mathbf{L}\beta}$ are provided as

$$\mathbf{T}^{\mathbf{L}}=\sum_{\beta}\mathbf{T}^{\mathbf{L}\beta},\quad\eta^{\mathbf{L}}=\sum_{\beta}\eta^{\mathbf{L}\beta},\quad\psi^{\mathbf{L}}=\sum_{\beta}\psi^{\mathbf{L}\beta}. \tag{21}$$

2.3.1. Constitutive relations

Following the derivation of the balance laws, constitutive equations must be formulated to complete the model. These include expressions for the partial stresses $\mathbf{T}^{\mathbf{I}}$ and $\mathbf{T}^{\mathbf{L}}$, the seepage velocity $\mathbf{w}_{\mathbf{LI}}$, and the mass exchange rate $\hat{\rho}^{\mathbf{I}}$. To ensure consistency with thermodynamic principles, these relations are derived using the local Clausius–Duhem inequality, with the specific Helmholtz free energy $\psi^{\alpha}=\varepsilon^{\alpha}-\theta^{\alpha}\eta^{\alpha}$ as the energy potential.

The local form of the entropy inequality incorporates a Lagrange multiplier λ to enforce the saturation constraint. This inequality is written as

$$\begin{aligned}&\sum_{\alpha}\left\{-\rho^{\alpha}\left[\left(\psi^{\alpha}\right)_{\alpha}'+(\theta)_{\alpha}'\eta^{\alpha}\right]+\mathbf{T}^{\alpha}\cdot\mathbf{D}_{\alpha}-\frac{1}{\theta}\operatorname{grad}\theta\cdot\mathbf{q}^{\alpha}\right\}\\&-\hat{\rho}^{\alpha}\left(\psi^{\alpha}-\frac{1}{2}\mathbf{x}_{\alpha}'\cdot\mathbf{x}_{\alpha}'\right)-\hat{\mathbf{p}}^{\alpha}\cdot\mathbf{x}_{\alpha}'+\lambda\left(1-\sum_{\alpha}\mathrm{n}^{\alpha}\right)_{\mathbf{I}}'\geq 0.\end{aligned} \tag{22}$$

This inequality serves as a basis for deriving constitutive restrictions consistent with thermodynamic laws.

The Helmholtz free energy of the ice phase is assumed to depend on the right Cauchy–Green deformation tensor and temperature, while for each component β of the liquid phase, it is taken as a function of its density and temperature

$$\psi^{\mathbf{I}}=\psi^{\mathbf{I}}(\mathbf{C}_{\mathbf{I}},\theta),\quad\psi^{\mathbf{L}\beta}=\psi^{\mathbf{L}\beta}(\rho^{\mathbf{L}\beta},\theta). \tag{23}$$

The rate of change of the Helmholtz energy for the ice is given by the chain rule expansion

$$\rho^{\mathbf{I}}(\psi^{\mathbf{I}})_{\mathbf{I}}'=2\rho^{\mathbf{I}}\mathbf{F}_{\mathbf{I}}\frac{\partial\psi^{\mathbf{I}}}{\partial\mathbf{C}_{\mathbf{I}}}\mathbf{F}_{\mathbf{I}}^{T}\cdot\mathbf{D}_{\mathbf{I}}+\rho^{\mathbf{I}}\frac{\partial\psi^{\mathbf{I}}}{\partial\theta}(\theta)_{\mathbf{I}}'. \tag{24}$$

This expression reflects how the energy varies due to mechanical deformation and thermal effects in the solid matrix. Similarly, for each liquid component, the variation is given by

$$\left(\psi^{\mathbf{L}\beta}\right)_{\beta}'=\frac{\partial\psi^{\mathbf{L}\beta}}{\partial\rho^{\mathbf{L}\beta}}(\rho^{\mathbf{L}\beta})_{\beta}'+\frac{\partial\psi^{\mathbf{L}\beta}}{\partial\theta}(\theta)_{\beta}'. \tag{25}$$

This decomposition separates contributions from changes in mass and thermal effects for the fluid components. After substituting the energy derivatives into the entropy inequality and applying standard procedures of continuum thermodynamics, the following expressions are obtained for the stresses. The energy-conserving parts of the stress tensors for ice and liquid take the form

$$\begin{aligned}&\mathbf{T}^{\mathbf{I}}=-\mathrm{n}^{\mathbf{I}}\lambda\left(\frac{(\rho^{\mathbf{IR}})_{\mathbf{I}}'}{\rho^{\mathbf{IR}}}\right)\mathbf{I}+2\rho^{\mathbf{I}}\mathbf{F}_{\mathbf{I}}\frac{\partial\psi^{\mathbf{I}}}{\partial\mathbf{C}_{\mathbf{I}}}\mathbf{F}_{\mathbf{I}}^{T},\\&\mathbf{T}^{\mathbf{L}}=-\mathrm{n}^{\mathbf{L}}\lambda\mathbf{I}.\end{aligned} \tag{26}$$

The first term in the ice stress represents an isotropic contribution due to the saturation constraint, while the second accounts for elastic deformation energy. The stress in the liquid is purely isotropic and driven by λ. The Lagrange multiplier λ, which enforces the saturation condition, is computed using the constitutive response of the liquid phase

$$\lambda = -\rho^{\mathbf{LR}} \left(\sum_{\beta} \frac{\partial \psi^{\mathbf{L}\beta}}{\partial \rho^{\mathbf{L}\beta}} + \frac{1}{\rho^{\mathbf{L}\beta}} \psi^{\mathbf{L}\beta} \right). \tag{27}$$

The specific entropy for each phase follows directly from the free energy dependence on temperature

$$\eta^{\mathbf{I}} = -\frac{\partial \psi^{\mathbf{I}}}{\partial \theta}, \quad \eta^{\beta} = -\frac{1}{\rho^{\mathbf{L}\beta}} \frac{\partial \psi^{\mathbf{L}\beta}}{\partial \theta}. \tag{28}$$

The dissipative parts of the constitutive relations describe irreversible phenomena. Phase change between ice and liquid is governed by the following rate law

$$\hat{\rho}^{\mathbf{I}} = -\delta_{\mu^{\mathbf{I}}} (\mu^{\mathbf{I}} - \mu^{\mathbf{L}}), \tag{29}$$

where the exchange is driven by the chemical potential difference between phases. The chemical potentials themselves are defined through

$$\mu^{\mathbf{I}} = \psi^{\mathbf{I}} + \frac{\lambda}{\rho^{\mathbf{IR}}}, \quad \mu^{\mathbf{L}} = \psi^{\mathbf{L}} + \frac{\lambda}{\rho^{\mathbf{LR}}}. \tag{30}$$

Momentum exchange between fluid components and the solid is described by

$$\hat{\mathbf{p}}^{\beta} = \mathrm{w}^{\mathbf{L}\beta} \lambda \operatorname{grad} n^{\mathbf{L}} - \delta_{\mathbf{w}_{\beta\mathbf{I}}} \mathbf{w}_{\beta\mathbf{I}}. \tag{31}$$

The term involving $\operatorname{grad} n^{\mathbf{L}}$ accounts for the volumetric redistribution due to saturation. Finally, heat conduction is governed by Fourier's law with an effective thermal conductivity

$$\mathbf{q} = -\alpha_{\nabla\theta} \operatorname{grad} \theta. \tag{32}$$

2.4. Numerical treatment

After the establishment of all fundamental assumptions, constitutive laws, and governing equations, the corresponding weak formulations must be derived to enable the numerical resolution of the field variables. The relevant unknowns, which vary both spatially and temporally, are collectively denoted as follows:

$$\mathcal{R} = \mathcal{R}(\mathbf{x}, \mathbf{t}) = \left\{ \mathbf{u}_{\mathbf{I}}, \mathbf{n}^{\mathbf{I}}, \mathrm{S}^{\mathrm{Bulk}}_{\mathrm{Macro}}, \mathrm{p}^{\mathbf{LR}}, \theta \right\}. \tag{33}$$

To facilitate the numerical solution, the standard Galerkin Finite Element Method (FEM) [12] has been employed. Through this method, the weak formulations are systematically obtained for each of the governing balance equations. These include the mass balance for the ice phase, the mass conservation for the overall mixture, the salinity transport equation for bulk brine, the momentum balance for the mixture, and the internal energy conservation for the entire multiphase system. The individual variational forms are elaborated below.

- $$\int_{\mathbf{B_I}} \left\{ \left(\mathrm{n}^{\mathbf{I}}\right)'_{\mathbf{I}} \rho^{\mathbf{IR}} + \mathrm{n}^{\mathbf{I}} \left(\rho^{\mathrm{IR}}\right)'_{\mathbf{I}} \mathrm{tr}_{\mathbf{I}} - \hat{\rho}^{\mathbf{I}} \right\} \delta \mathrm{n}^{\mathbf{I}} \mathrm{dv} = 0, \tag{34}$$

- $$\int_{\mathrm{B_I}} \left\{ \mathrm{n}^{\mathrm{L}} \left(\mathrm{S}^{\mathrm{br}}\right)'_{\mathbf{I}} + \left(\mathrm{n}^{\mathrm{L}}\right)'_{\mathbf{I}} \mathrm{S}^{\mathrm{br}} + \frac{\mathrm{n}^{\mathrm{L}}}{\rho^{\mathrm{LR}}} \mathrm{S}^{\mathrm{br}} \left(\rho^{\mathrm{LR}}\right)'_{\mathbf{I}} + \mathrm{n}^{\mathbf{L}} \mathrm{S}^{\mathrm{br}} \mathrm{tr} \mathbf{D}_{\mathbf{I}} \right\} \delta \mathrm{S}^{\mathrm{bulk}}_{\mathrm{Macro}} \mathrm{dv} - \int_{\mathrm{B_I}} \left\{ \frac{\mathbf{j}^{\mathrm{L}.}}{\rho^{\mathrm{LR}}} \cdot \operatorname{grad} \delta \mathrm{S}^{\mathrm{bulk}}_{\mathrm{Macro}} \right\} \mathrm{dv} = \int_{\partial \mathrm{B}_{\mathbf{I}}} \left\{ \frac{\mathbf{j}^{\mathrm{L.s}}}{\rho^{\mathrm{LR}}} \delta \mathrm{S}^{\mathrm{bulk}}_{\mathrm{Macro}} \cdot \mathbf{n} \right\} \mathrm{da}, \tag{35}$$

- $$\int_{\mathrm{B_I}} - \left\{ \mathrm{n}^{\mathbf{L}} \mathbf{w}_{\mathrm{LI}} \cdot \operatorname{grad} \delta \mathrm{p}^{\mathbf{LR}} \right\} \mathrm{dv} + \int_{\mathrm{B_I}} \left\{ \mathrm{tr}\, \mathbf{D}_{\mathrm{I}} + \sum_{\alpha} \frac{\mathrm{n}^{\alpha}}{\rho^{\alpha \mathrm{R}}} \left(\rho^{\alpha \boldsymbol{R}}\right)'_{\mathbf{I}} - \hat{\rho}^{\mathbf{I}} \left(\frac{1}{\rho^{\mathrm{LR}}} - \frac{1}{\rho^{\mathrm{IR}}} \right) \right\} \delta \mathrm{p}^{\mathbf{LR}} \mathrm{dv} = - \int_{\partial \mathrm{B}_{\mathrm{I}}} \left\{ \mathbf{n}^{\mathbf{L}} \mathbf{w}_{\mathrm{LI}} \delta \mathrm{p}^{\mathbf{LR}} \cdot \mathbf{n} \right\} \mathrm{da}, \tag{36}$$

- $$\int_{\mathrm{B_I}} \left(\sum_{\alpha}^{\mathbf{IL}} \mathbf{T}^{\alpha} \right) \cdot \operatorname{grad} \delta \mathbf{u}_{\mathrm{I}} \mathrm{dv} - \int_{\mathrm{B_I}} \left(\sum_{\alpha}^{\mathbf{IL}} \rho^{\alpha} \right) \mathbf{b} \cdot \delta \mathbf{u}_{\mathrm{I}} \mathrm{dv} = \int_{\partial \mathrm{B}_{\mathbf{I}}} \left\{ \mathbf{t} \cdot \delta \mathbf{u}_{\mathrm{I}} \right\} \mathrm{da}, \tag{37}$$

- $$\int_{\mathbf{B_I}} \left\{ \theta \rho^{\mathbf{I}} \left(\eta^{\mathbf{I}}\right)'_{\mathbf{I}} \right\} \delta\theta \mathrm{dv} + \int_{\mathrm{B_I}} \left\{ \theta \rho^{\mathrm{L}} \left(\eta^{\mathrm{L}}\right)'_{\mathbf{L}} \right\} \delta\theta \mathrm{dv} - \int_{\mathrm{B_I}} \{ \mathbf{q} \cdot \operatorname{grad} \delta\theta \} \mathrm{dv} + \int_{\mathrm{B_I}} \left\{ \hat{\mathbf{p}}^{\mathbf{I}}_{\mathrm{E}} \cdot \mathbf{w}_{\mathbf{LI}} \right\} \delta\theta \mathrm{dv} + \int_{\mathrm{B_I}} \left\{ \hat{\rho}^{\mathbf{I}} \left[\mathbf{h}^{\mathbf{L}} - \mathbf{h}^{\mathbf{I}} \right] \right\} \delta\theta \mathrm{dv} = \int_{\partial \mathrm{B}_{\mathbf{I}}} \{ \mathbf{q} \delta\theta \cdot \mathbf{n} \} \mathrm{da}. \tag{38}$$

The resulting system of equations constitutes a fully coupled framework governing the macroscopic behavior of the sea ice matrix under thermal, mechanical, and transport processes. This eTPM based homogenization framework is capable of resolving the evolution of state variables under external forcing and internal phase transformations.

Nonetheless, it must also be acknowledged that the fundamental mechanisms responsible for ice formation stem from microscale thermodynamic and morphological processes, including the phase transition between brine and ice, brine channel formation, and the emergence of separated pores. These microscale features are not directly captured within the macroscopic formulation presented above. Therefore, a more detailed description that incorporates microscale pattern formation is provided in Section 2.5, where a coupled phase-field model involving salinity and an order parameter field is introduced to describe the interfacial dynamics between saline liquid and growing ice.

2.5. Phase field solidification

A phase field solidification model is developed following [67] to simulate the microscale growth dynamics of sea ice. The phase field model describes first order phase transitions in the framework of Landau–Ginzburg theory [77], with dynamical pattern formations that are consistent with the thermodynamics of freezing processes. A modified microscopic model will be used in Section 2.6 to derive the macroscopic sea ice growth rates. Due to the much faster microscopic processes compared to the macroscopic scale, the microscopic equilibrium states of the brine channels can be used for the coupling because of the Tikhonov theorem [78].

2.5.1. Coupled model for salinity and order parameter evolution

To model seawater thermodynamics, the interaction between salt and ice is described using the Landau–Ginzburg functional $\Omega_{LG} = \int \omega_{LG}\, d L_{Micro}$, which includes both potential and gradient energy contributions:

$$\omega_{LG} = \underbrace{\frac{1}{4}(a \mathrm{n}^{\mathbf{I}}_{\mathrm{Micro}})^4 - \frac{1}{2}(a \mathrm{n}^{\mathbf{I}}_{\mathrm{Micro}})^3 + \left(\frac{1}{4} - \frac{1}{2} \left(m - \frac{1}{2}\sigma \right) \right) (a \mathrm{n}^{\mathbf{I}}_{\mathrm{Micro}})^2 + \frac{\beta_1}{2}\sigma^2}_{\omega_L} + \underbrace{\frac{1}{2} L_c^2 \left(\frac{\partial a \mathrm{n}^{\mathbf{I}}_{\mathrm{Micro}}}{\partial L_{Micro}} \right)^2}_{\omega_G}, \tag{39}$$

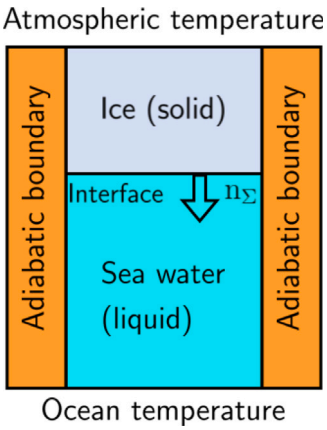

Fig. 3. Conceptual diagram showing 1-D moving interface.

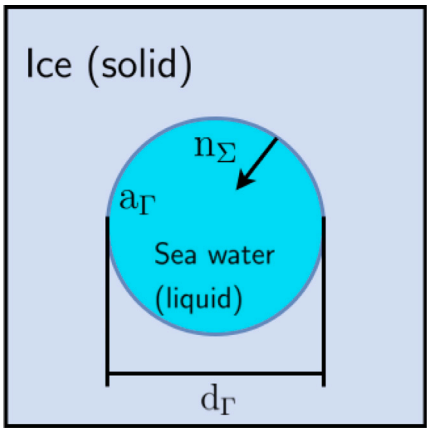

Fig. 4. Schematic representation of ice and seawater interface with idealized pore diameter d_Γ, area a_Γ and normal direction of gradient of temperature n_Σ looking inwards to the pore.

The parameter $m = \frac{1}{2}\frac{T_0 - T}{T_0 - T_s}$ is offset by $\frac{1}{2}\sigma$ to account for the freezing point depression caused by salinity, where T_0 and T_s are the melting point of pure water and the lowest supercooling temperature, respectively. The order parameter $n^{\mathbf{I}}_{\text{Micro}}$ lies between 0 and 1. The characteristic length L_c is the doubled critical radius of a nucleated ice structure. If the critical radius of a nucleus is known, the length z can be determined from the dimensionless length ζ with $z = L_c\zeta$ where L_c is the double critical radius, L_c can be determined from classical nucleation theory

$$L_c = \frac{4\gamma T_0}{\rho_{ice}\hat{q}(T_0 - T_s)}. \tag{40}$$

Further details on the derivation of microscale field equations, and their critical points can be found in Appendix A.2. Substituting typical values of constants $\rho_{ice} = 0.917\ \frac{\text{g}}{\text{cm}^3}$ [79], $\hat{q} = 3.33 \times 10^9\ \frac{\text{erg}}{\text{g}}$ [80], $\gamma = 29\ \frac{\text{erg}}{\text{cm}^2}$ [80], $T_0 = 273.15$ K, and $T_s = 236.6$ K, we find $L_c = 2.84$ nm [81]. For a bath temperature of -1 °C, the freezing velocity $c = 10^2\ \frac{\mu\text{m}}{\text{s}}$ [82] gives a characteristic time scale $t_0 = \frac{L_c}{c} = 0.0284$ ms.

The model is solved using Exponential Time Differencing of second order (ETD2) [83] coupled with spectral spatial discretizations in the Fourier space [84]. By representing the spatial derivatives in Fourier space, the developed algorithm exploits the efficiency and accuracy of spectral methods, which are particularly suitable for periodic domains and smooth solutions. ETD2 in the temporal domain precisely handles the stiff linear terms in the evolution equations, enabling stable and accurate integration over large time steps. This coupling is well-suited for phase field models of solidification, as it preserves sharp interface dynamics and captures complex nonlinear interactions inherent to Landau–Ginzburg equations. The approach offers the potential of an effective framework suitable for simulations that involve longer times and complex morphological evolution in solidification phenomena. A more detailed discussion of the scaling factors between dimensionless and dimensional quantities can be found in [85].

2.6. Micro-macro coupling

The macroscale phase transition phenomena occur as a result of a 1D moving interface between ice and water. Fig. 3 represents the idea of the moving front.

The interfacial mass transfer is defined as a function of heat fluxes and latent heats of ice and water, and the normal vector of gradient of temperature

$$\hat{\rho}^{\mathbf{I}} = \frac{(\mathbf{q}^{\mathbf{L}} - \mathbf{q}^{\mathbf{I}}) \cdot \mathbf{n}_\Gamma}{(\mathrm{h}^{\mathbf{L}} - \mathrm{h}^{\mathbf{I}})}, \tag{41}$$

Combining Eqs. (41) and (A.24), the continuum mass transfer can be read as

$$\hat{\rho}^{\mathbf{I}} = a_\Gamma \frac{(\mathbf{q}^{\mathbf{L}} - \mathbf{q}^{\mathbf{I}}) \cdot \mathbf{n}_\Gamma}{(\mathrm{h}^{\mathbf{L}} - \mathrm{h}^{\mathbf{I}})}. \tag{42}$$

This leads to the coupling in graphical form as shown in Fig. 5. Further details on the derivation of interfacial mass transfer term can be found in Appendix A.3.

2.6.1. Pore area and volume fraction

The pore diameter d_Γ is assumed to be the part of the 1-D length on the microscale that is not filled with ice. Since the pore diameter depends on the distribution of ice and liquid phases, it can be written with respect to the microscale volume fraction $n^{\mathbf{I}}_{\text{Micro}}$. As will be shown in Section 3.1, (cf. Fig. 8), the pore diameter d_Γ can be written as a sigmoid function of the microscale volume fraction. The physical interpretation is that when the entire 1-D length is filled with water with no freezing occurrence, the pore diameter is maximum and equal to the size of the 1-D length. As water starts freezing, the pores get smaller, hence, decreasing the pore diameter. The general form of the sigmoid relation is given as

$$d_\Gamma = f\left(n^{\mathbf{I}}_{\text{Micro}}\right) = a_4 + (a_1 - a_4) \times \exp\left(-\exp\left(-a_2 \times \left(n^{\mathbf{I}}_{\text{Micro}} - a_3\right)\right)\right). \tag{43}$$

Following [86,87], the interfacial area a_Γ can also be written as a function of saturation or porosity of the porous medium, or in other words the volume fraction $n^{\mathbf{I}}_{\text{Micro}}$

$$a_\Gamma = a_\Gamma(n^{\mathbf{I}}_{\text{Micro}}). \tag{44}$$

Assuming circular pore area, the area in Eq. (44) can be easily determined as

$$a_\Gamma = \frac{\pi d_\Gamma^2}{4}. \tag{45}$$

The idea of circular pores with moving interfaces can be perceived in Fig. 4.

This yields an offline coupling scheme (cf. Fig. 5) where the information of temperature and salinity is passed from the macroscale while pore diameter and energy is transferred back from the microscale through the pore area. The growth rate of ice $\hat{\rho}^{\mathbf{I}}$ finds itself appearing in mass balance of ice (34), mixture (36) and energy balance of the mixture (38), hence affecting the ice volume fraction $n^{\mathbf{I}}$, pore pressure $p^{\mathbf{LR}}$ and the temperature θ, respectively.

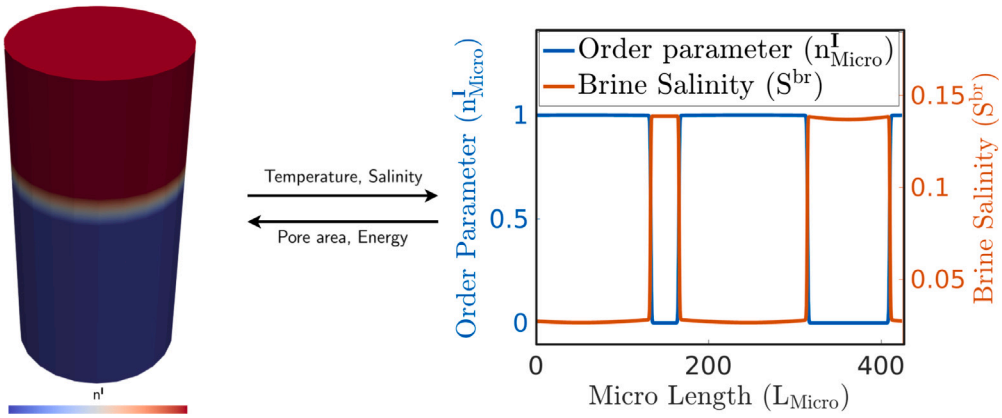

Fig. 5. Schematic representation of proposed micro-macro linking scheme between macroscale and microscale phase transition with arrows showing information exchange between the scales.

Table 1
Microscale parameters.

Parameter	Value	Unit
Freezing temperature T_0	273.15	K
Supercooling temperature T_s	236.6	K
Ambient temperature T	270	K
q	1	–
τ_1	10	–
τ_0	$\frac{1}{100}$	–

3. Results and discussion

In this section, the simulation results generated by the multiscale framework developed in the preceding section are presented and analyzed. The presentation is structured such that the behavior at each scale is first isolated before their coupled interaction is demonstrated. To begin, the outcomes of the standalone microscale phase-field model are explored in Section 3.1, through which the process of phase separation, salt rejection into pores, and the establishment of an equilibrium relationship between temperature and ice volume fraction are illustrated. The justification for the sigmoid function used to link pore diameter to the macroscale is provided by this microscale analysis. Subsequently in Section 3.2, the results from the fully coupled multiscale simulation are presented, showing the temporal evolution of the ice front, along with vertical profiles of temperature, salinity, and ice volume fraction within a macroscopic domain. A critical analysis of how these microscale dynamics directly influence macroscale behavior is then provided in the discussion, where the role of the evolving pore area in regulating the ice growth rate is highlighted and the multiscale model's performance is compared to scenarios with fixed pore geometry. Finally, the section ends with a discussion on the skills of the model and potential future directions of improvement.

3.1. Microscale phase transitions

A 1-d simulation is set up to simulate the temperature and salinity evolution at the microscale. The simulation parameters and constants are summarized in Table 1.

The initial conditions for the order parameter are set to be slightly lower than $n^{I}_{Micro} = 0.5$ with minor perturbations across the length and the salinity is chosen to be $\sigma = 0.0606$ which corresponds to the bulk salinity of the ocean 35 $\frac{g}{kg}$ as shown in the 6 and 6(a). The temporal evolution of order parameter leads to phase separation with salt rejection into pores. The pore space can be determined by regions where $n^{I}_{Micro} = 0$. The pore space ultimately becomes highly concentrated and no salt is present in regions where $n^{I}_{Micro} = 1$. It is also worth noting in Fig. 6(b) that, even though the initial condition placed only two 'seeds' for dendritic pattern formation, a third ice region eventually forms before reaching an equilibrium state at $\tau = 1000$.

However, on the macroscale, the temperature ranges are large and hence the dependence of order parameter over temperature is needed for a wider range before upscaling to the macroscale TPM formulation. The microscale information is interpreted at the Gauss point level on the macroscale and therefore and single value instead of a distribution over length is required. This is done by averaging over the length, yielding the mean value for a particular temperature

$$n^{I}_{Micro}(\theta) = \frac{\sum n^{I}_{Micro}(\tau_{end})}{N}, \tag{46}$$

where N denotes the number of elements on the 1-D microlength. The range of temperatures is simulated resulting in a distribution of microscale volume fraction with respect to the temperature. The behavior is in good agreement with the classical first order phase transition according to the Landau–Ginzburg theory and is presented in Fig. 7.

Converting the dimensionless quantities to dimensions, for an ambient temperature of 270 K, the pore diameter is calculated as 119.82 μm, the total time for pattern formation as 0.022 ms and a maximum salinity inside concentrated pores to be 79.16 ppt. The results are well in line with experimental literature on sea ice for brine channel size [88], and salinity [89].

The calculation of interfacial pore diameter d_Γ over temperature follows from the distribution of ice and liquid phases over the length. In case of a completely liquid domain ($n^{I}_{Micro} = 0$), the pore diameter is equal to the total length of the 1-D control length and for a completely ice filled domain ($n^{I}_{Micro} = 1$), the pore diameter is zero. The dependence of pore diameter over volume fraction is shown in Fig. 8.

The sharp jump in the simulated plot is due to the reason that at a certain threshold temperature, and consequently volume fraction, the patterns stop forming and the phases exist completely separate. Such sharp jumps are not seen on the macroscale, and hence, a smooth sigmoid function is used to fit the simulated curve. Following Eq. (43), the expression for the pore diameter with coefficient values is given as

$$d_\Gamma = f\left(n^{I}_{Micro}\right) = -1.2582 + (196.7638 + 1.2582) \times \exp\left(-\exp\left(3.3443 \times \left(n^{I}_{Micro} - 0.3925\right)\right)\right). \tag{47}$$

The curve fit is chosen deliberately to represent the microscale growth in order to reduce computational effort since the problem is not of highly dynamic nature and several nodes during the simulation process encounter same/ similar temperature and salinity values. Solving the microscale equation on these nodes would be (i) very

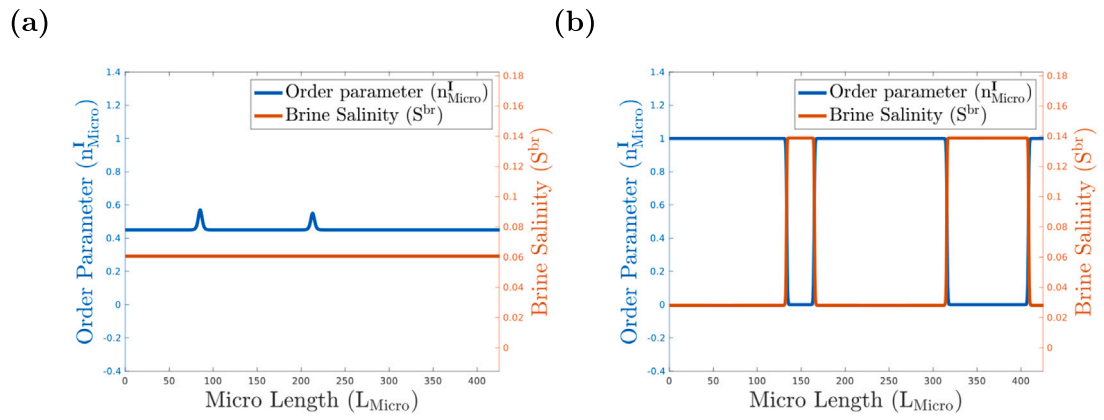

Fig. 6. Temporal evolution of order parameter and salinity at $T_m = 270$ K for **(a)** $\tau = 0.001$ and **(b)** $\tau = 1000$.

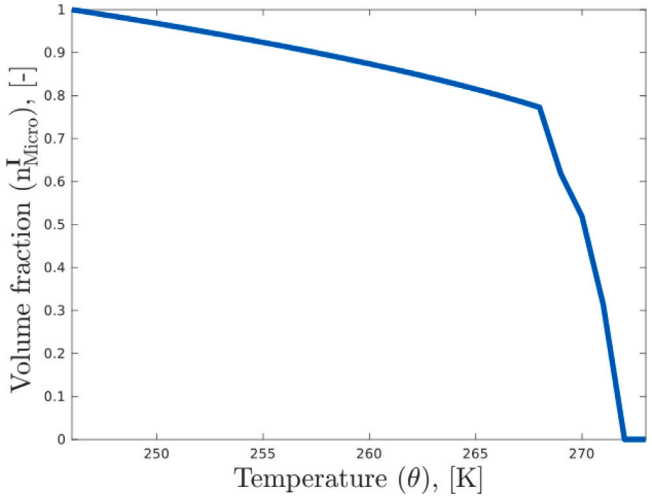

Fig. 7. Dependence of Volume fraction on Temperature.

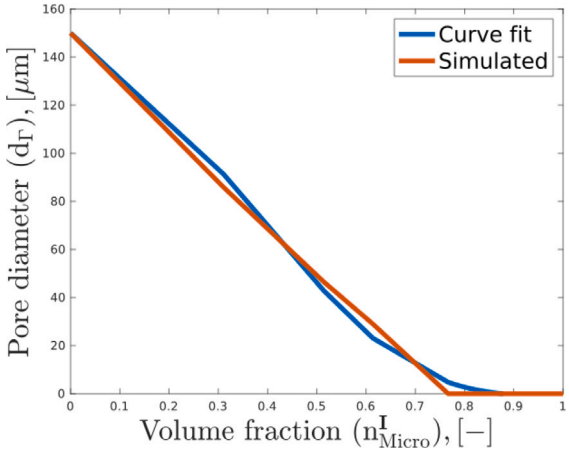

Fig. 8. Simulated and curve fitted pore diameter d_Γ.

time consuming and (ii) redundant, and (iii) reach same values of resolved pore area. This is due to (i) the microscale simulation always reach an equilibrium state in the order of microseconds which is much lower than the time step size on the macroscale (seconds or hours), and (ii) currently an isotropic growth model is implemented on the microscale, meaning that the simulation will always reach the same equilibrium state for given initial conditions. Therefore, it was decided to re-implement and switch to an offline coupling scheme instead of online where both scales are resolved simultaneously.

3.2. Macroscale phase transitions

For the macroscale simulations, a cylindrical domain is assumed considering the typical ice core geometries used for experiments. The height and diameter of the cylindrical core are $h = 1.0$ m and $d = 0.5$ m, respectively. A dirichlet boundary condition of temperature is prescribed at the nodes on the top surface shown by red dots in Fig. 9$_a$. The only prescribed boundary condition is that of temperature considering the physical condition of a warmer ocean with cold atmosphere on top. The prescribed temperature on the top nodes is $\theta = 262.15$ K $= -11$ °C. The time step size during the simulation was chosen to be $\Delta t = 1$ h. Results are observed along the height of the ice column in the center as shown in Fig. 9$_b$ to analyze verticle evolution of variables.

Initial conditions for domain temperature, volume fraction, and bulk salinity are $\theta_0 = 272.15$ K $= -1$ °C, $n^{I}_0 = 0.1[-]$, and $S^{bulk}_{Macro_0} = 35\ \frac{g}{kg}$, respectively. Although not prescribed directly, but due to its dependence on temperature, the initial brine salinity S^{Br} in the domain is $S^{Br} = 20.53$ ppt and on the top nodes is $S^{Br} = 150.82$ ppt.

The moving ice front follows the normal direction n_Γ of the temperature gradient and evolves initially in both vertical and radial directions based on Eqs. (47), (45), and (42). Once the radial boundaries are reached, the outward normal of the gradient only points towards the depth, and hence, the ice- water interface follows further in the vertical direction. The temporal evolution of ice volume fraction over the domain can be observed in Fig. 10 (a-f).

Evolution of remaining field quantities like temperature θ, ice n^{I} and brine n^{L} fractions, and brine S^{br} salinity over height are presented in Fig. 11. The results are in good agreement with observed values in the sea ice literature, cf. [10,90].

Due to growing ice, pores within the ice matrix start becoming smaller. The concentration of brine trapped within these pores increases, hence restricting the further growth of ice. Reduction in available pore space also leads to reduced macroscale ice growth rate $\dot{\rho}^{I}$, as shown in Fig. 12.

This behavior leads to different types of regions in the domain, completely ice-filled regions where the freezing process has stopped, transition regions filled with pores and high freezing rates, and water-filled regions where the temperature and still for the freezing process to start (see Fig. 13). The microscale instances of phase transition within the macroscale can be visualized in Fig. 14. Furthermore, the influence of pore area on ice growth rate is analyzed. In this case, the microscale influence is decoupled and fixed a_Γ values are assigned throughout the domain. These are then compared to the multiscale growth model, where microscale influence is also evaluated. It is observed that the reduction in a_Γ leads to inhibited ice growth. Over the course of the

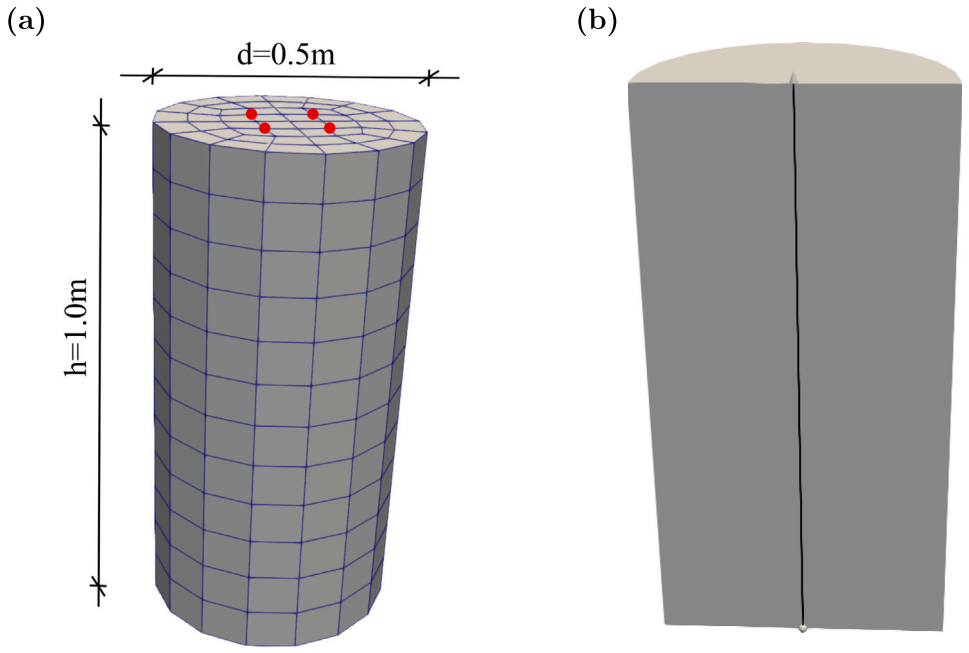

Fig. 9. Model setup. **(a)** Domain and boundary conditions. **(b)** Centerline along the z-direction to analyze vertical profiles.

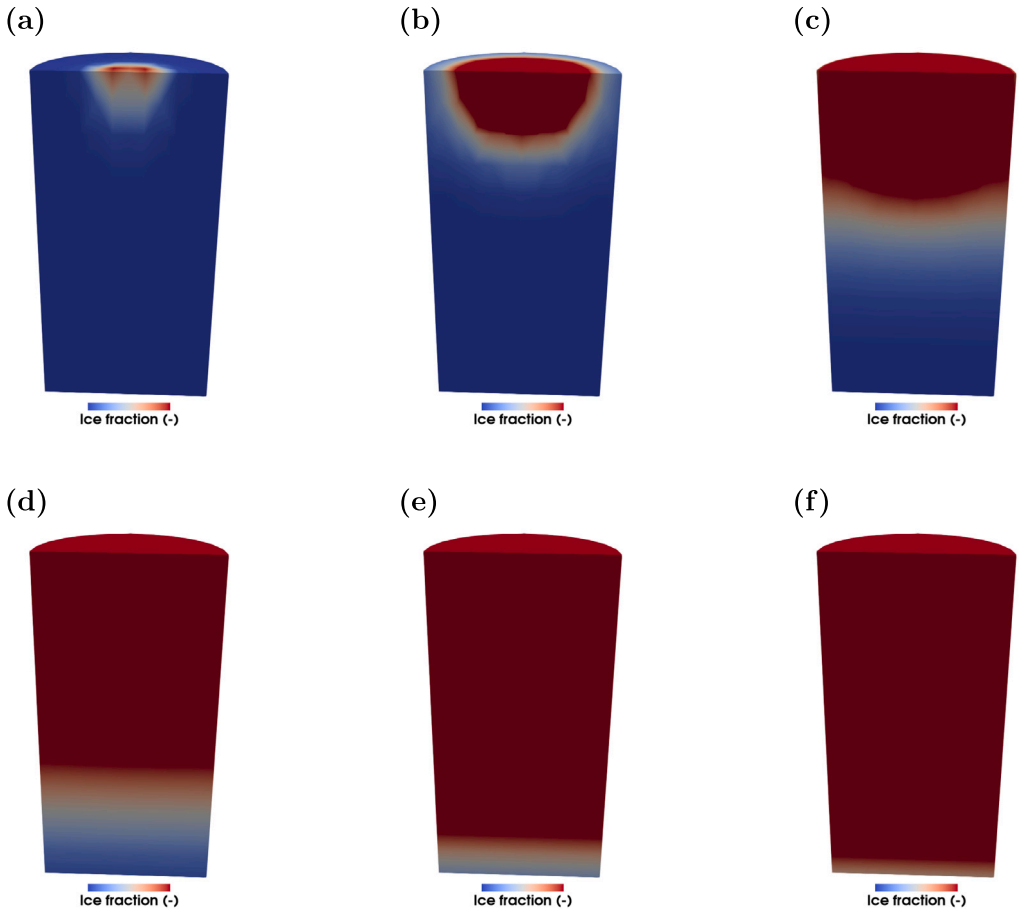

Fig. 10. Evolution of homogenized macroscale ice volume fraction over time. Red represents increasing ice fraction in the domain. **(a)** $t = t_0$. **(b)** $t = 3$ h. **(c)** $t = 10$ h. **(d)** $t = 20$ h. **(e)** $t = 30$ h. **(f)** $t = 40$ h.

simulation, it is seen that even for similar initial pore sizes in varying a_Γ and constant $a_\Gamma = 10$ mm, the evolution behavior is different as the simulation evolves.

While translating complex high-fidelity small-scale process-based models presents a significant computational challenge, our multiscale modeling framework incorporates several strategies to enhance

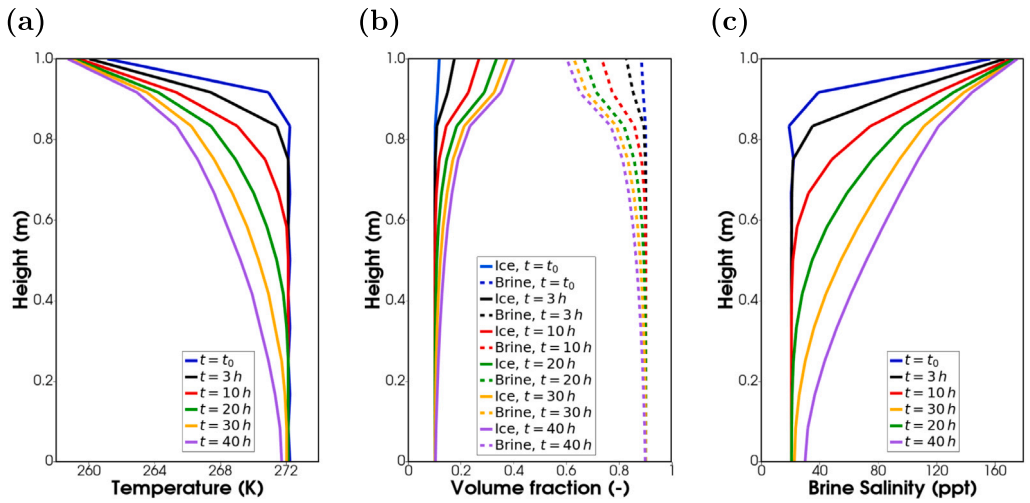

Fig. 11. Evolution of field quantities over time. **(a)** Temperature, θ. **(b)** Volume fractions of ice and brine. **(c)** Brine salinity, S^{Br}.

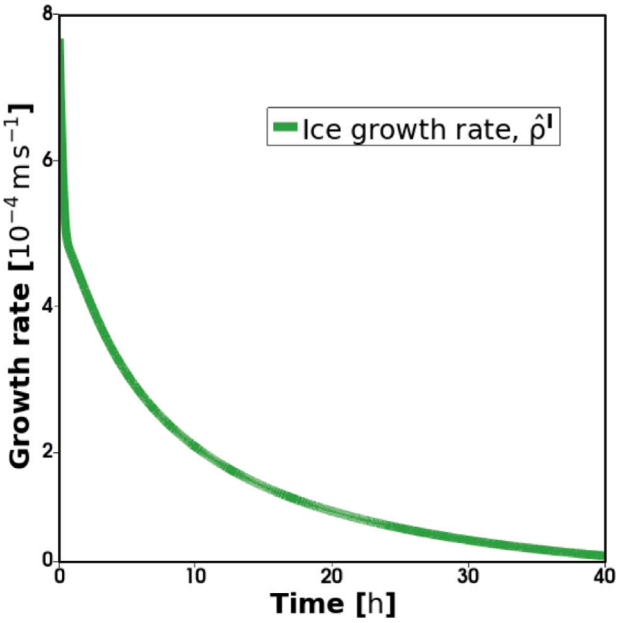

Fig. 12. Temporal evolution of ice growth rate $\hat{\rho}^{\mathbf{I}}$.

computational efficiency. A key consideration is the judicious use of Exponential Time Differencing Schemes (ETD2). Using ETD2 for temporal and Fourier space for spatial discretization offer a distinct advantage by allowing for the efficient solution of very fine steps on the microscale. This not only maintains high accuracy for rapid microscale dynamics but also significantly reduces the computational burden often associated with explicit methods that would require impractically small time steps to ensure stability. The strength of ETD2 lies in its ability to handle stiff terms exactly, making it particularly well-suited for the complex, potentially fast-evolving processes at the microscale. Fourier space discretization makes it possible to resolve finer spatial dynamics such as sharp ice-brine interface at reduced computational effort.

Furthermore, to avoid redundantly solving numerous initial boundary value problems at the microscale, the micro- and macro- scales are coupled in an offline manner. This approach involves using a pre-computed function to represent microscale effects, rather than requiring a full online solver at each temporal and spatial step. The inherent advantage of offline coupling over a full field online coupling is obvious. A full online coupling would necessitate running a detailed microscale simulation at every macroscale grid point and time step. This would lead to an exorbitant computational cost due to the sheer number of redundant simulations that would need to be performed, as many microscale behaviors might be similar across different macroscale Gauss points or evolve slowly enough that constant re-computation is unnecessary. Initial tests were performed with an online full field coupling between scales and the impracticality of the approach eventually rendered itself out of the scope and discussion in this paper. Therefore, an offline coupling strategy effectively bypasses this computational bottleneck by encapsulating the microscale behavior into a curve fitted function. The function can be queried quickly, thereby offering substantial savings and making the entire framework feasible for larger-scale applications. Due to lack of availability of other works, a comparative analysis of computational efficiency of various models could not be performed.

Future development of this multiscale framework will focus on two key areas, namely, rigorous validation and the derivation of physically based parameterizations for large scale models. The next crucial step is to validate the predictions of our model against controlled laboratory experiments, such as those conducted by Zhen et al. [91], which provide high-fidelity data on ice growth rates and bulk salinity under precisely defined thermal and salinity conditions. While the experimental study by Zhen et al. [91] provides crucial macroscale data on ice growth, our model distinguishes itself by simulating the fundamental microscale processes, such as pore scale ice-brine phase separation, that produce these observable outcomes. Successfully replicating these empirical results through appropriate parameterizations will confirm the fidelity of our microscale physics. Furthermore, while our model is computationally intensive for direct use in global climate simulations, its strength lies in its potential to inform and improve the parameterizations used in ocean general circulation models (OGCMs). Current models revolving around sea ice descriptions differ in objectives and also one or more of several key variables that affect the sea ice system. For example, the work of Toyoda et al. [92] attempts at improving sea ice representation in climate models at large scale by incorporating variable salinity parameterizations. In contrast to this, the presented approach does not focus on snow and melt pond dynamics, but explicitly resolves the coupled phase-field and porous media physics to derive these behaviors from a more fundamental basis. The framework can be used to derive more robust, process based inferences that capture the underlying physics of pore formation and brine entrapment. This approach creates a powerful, vertically integrated research

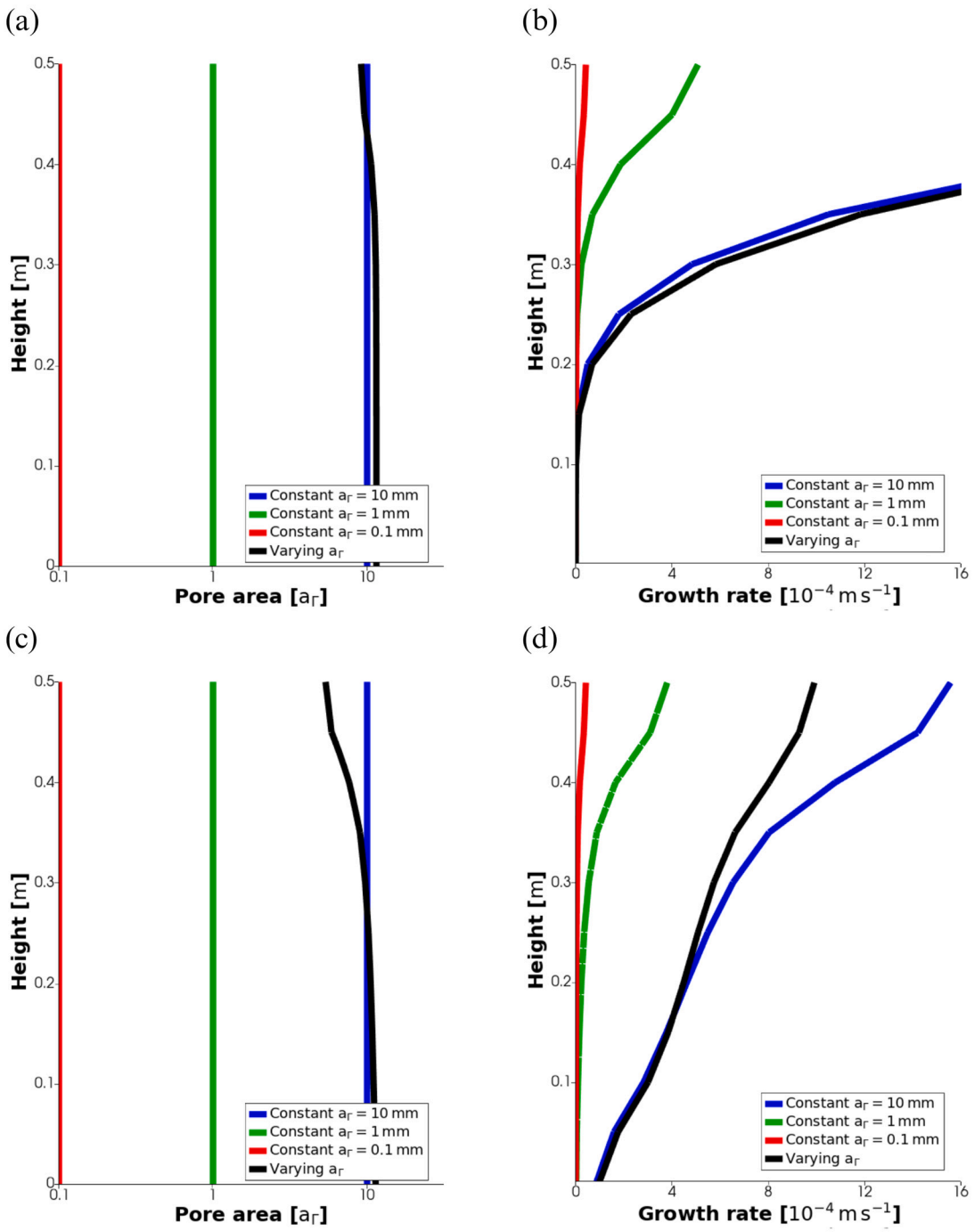

Fig. 13. Analysis of pore area and its effect on ice growth rate over time. **(a)** Pore area distribution over height at $t = t_0$. **(b)** Ice growth rate distribution over height at $t = t_0$. **(c)** Pore area distribution over height at $t = 40$ h. **(d)** Ice growth rate distribution over height at $t = 40$ h.

pathway, bridging fundamental laboratory observations with detailed process modeling to ultimately enhance the predictive accuracy of global climate systems.

Translating such complex high-fidelity small-scale process-based models is also a challenge computationally. More recent models have attempted at reducing the computational cost by developing surrogates through machine learning and dimensionality reduction techniques in various contexts. Sea ice rheology parameters have been tuned using machine learning to tune the Bingham–Maxwell rheology (BBM) parameterization [93]. K-nearest neighbors (KNN) surrogate model was also used to predict sea ice concentration anomaly unto 90 days in advance [94]. Image processing has been quite popular recently to predict sea ice properties on both small [95] and large scales [96], including more recently, also internal and interfacial convection [97]. The MOSAiC expedition has also provided data for parametrization of various sea ice related quantities of interest [98]. Hybrid approaches that combine high- and low-fidelity models [99], and also machine learning and data assimilation [100] can prove to be useful for tackling the various fidelity and accuracy challenges separately.

Modeling and understanding of freezing processes within the ice, particularly in these transition regions and at multiple scales, is important since they also affect the marine biogeochemical activity by acting as habitats for ice algae and diatoms to survive during the harsh winter months, processes that have also been studied by combining

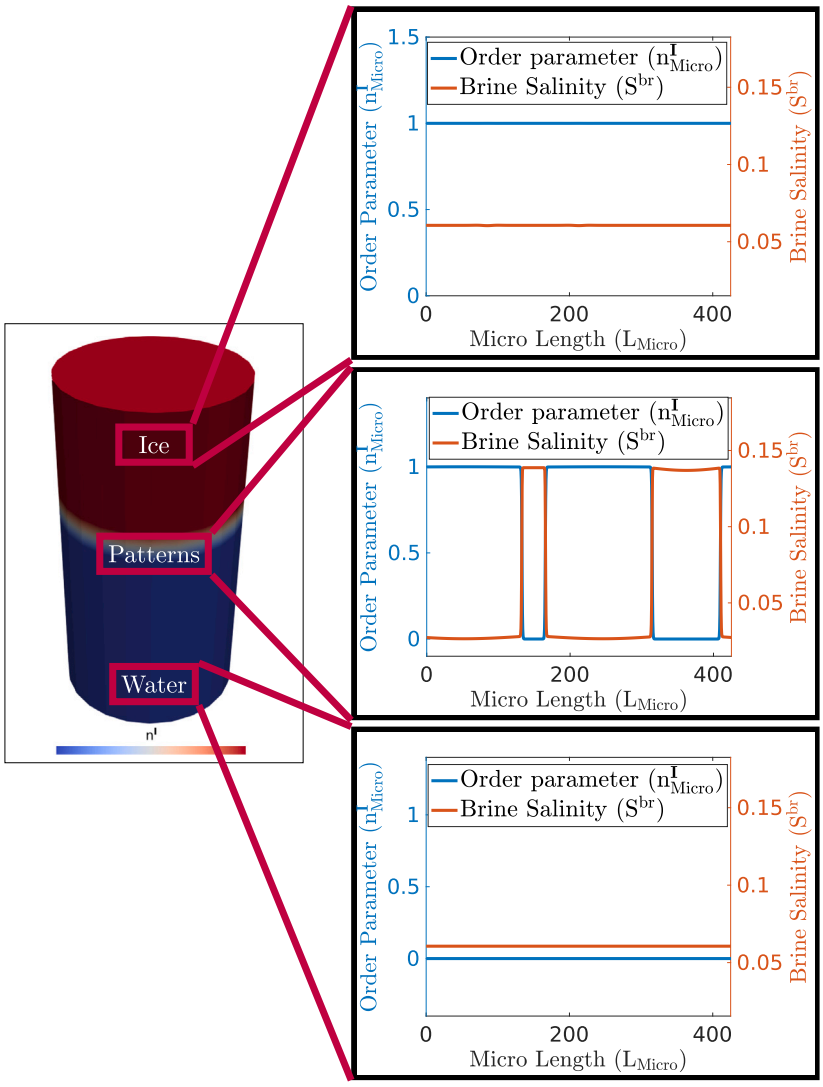

Fig. 14. Regions of ice, water and patterns depicted as part of resolved macroscale ice volume fraction.

them with TPM based formulations [61,63,101]. Microbial habitats also act as stressors by influencing the structure of sea ice through microbially induced convection [102] and inhibiting ice growth [103]. Such processes have not been included in the present study.

4. Conclusion

This paper presents and validates a multiscale framework to describe the complex thermodynamic processes governing the formation of new sea ice. By coupling the extended Theory of Porous Media (eTPM) at the macroscale with a temperature and salinity dependent phase-field model at the microscale, this work establishes a direct link between microstructural pattern formation and macroscopic sea ice evolution. The scales are effectively connected through an offline scheme where macroscale conditions of temperature and salinity inform the microscale simulations, which in turn provide a physically grounded function for the evolving pore area that governs phase change at the macroscale. The simulation results confirm the utility of this comprehensive modeling approach.

The primary strength of this framework lies in its ability to resolve the fundamental physics of ice formation across scales. The model successfully captures the critical microscale dynamics of phase separation, where salt is rejected from the growing ice matrix and becomes concentrated in liquid brine inclusions. A key finding from the coupled simulations is the crucial role of this evolving pore geometry in regulating the overall ice growth rate. By demonstrating that a dynamic pore structure leads to more realistic predictions compared to models assuming a fixed geometry, this work highlights the necessity of integrating microscale processes for accurate macroscale simulations. This work provides a insights about advantages of using varying multiscale pore space properties over more empirically parameterized approaches.

While the current framework provides a robust foundation, its development was guided by necessary simplifications that open clear avenues for future research. The present model assumes circular pores and isotropic crystal growth, whereas natural sea ice exhibits significant anisotropy. Therefore, the most critical next step is the development of a multiscale anisotropic model. This will involve modeling anisotropic crystal growth at the microscale and integrating an anisotropic crystal orientation tensor at the macroscale to simulate the ice growth characteristic of first-year sea ice. Building upon this improved physical structure, subsequent work will incorporate other important mechanisms not yet studied, such as convection dominated brine drainage, the effects of multiple solute species, and freezing point depression due to antifreeze proteins. These future enhancements will further increase the model's capabilities, paving the way for its use in developing more accurate parameterizations for large-scale climate models.

CRediT authorship contribution statement

Raghav Pathak: Conceptualization, Methodology, Software, Formal analysis, Investigation, Writing – original draft. **Seyed Morteza Seyedpour:** Project administration, Writing – original draft. **Bernd Kutschan:** Conceptualization. **Andrea Thom:** Conceptualization. **Silke Thoms:** Conceptualization, Funding acquisition, Supervision. **Tim Ricken:** Conceptualization, Funding acquisition, Supervision. All authors have read and agreed to the published version of the manuscript.

Ethics declaration

This study did not involve human or animal subjects, and thus, no ethical approval was required. The study protocol adhered to the guidelines established by the journal.

Declaration of competing interest

The authors declare that they have no known competing financial interests or personal relationships that could have appeared to influence the work reported in this paper.

Acknowledgments

This work was supported by the Deutsche Forschungsgemeinschaft (DFG), Germany in the framework of the priority program SPP 1158 "Antarctic Research with comparative investigations in Arctic ice areas" by the following grant 463296570 (Priority Programme SPP 1158, Antarctica). T.R. further thanks the Deutsche Forschungsgemeinschaft (DFG, German Research Foundation), Germany for supporting this work via the following projects: 312860381 (Priority Program SPP 1886, Subproject 12); 390740016 (Germany's Excellence Strategy EXC 2075/1); 436883643 (Research Unit Programme FOR 5151 (QuaLiPerF), Project P7); 327154368 (SFB 1313 Project C03 Vertebroplasty); 504766766 (Project Hybrid MOR); 465194077 (Priority Programme SPP 2311, Project SimLivA). TR is further supported by the Federal Ministry of Education and Research (BMBF, Germany) within ATLAS by grant number 031L0304A. RP is supported by the Add-on Fellowship of the Joachim Herz Foundation. All authors have read and agreed to the published version of the manuscript.

Appendix. Supplementary derivations

This section consists of some equations and derivations that might help the reader to get a deeper insight into the mathematical modeling aspects of the paper.

A.1. Kinematics in the framework of TPM

Each material point $\mathcal{P}$ from the body $\mathcal{B}$ is characterized by its spatial position $\mathbf{x}$. The collection of all such points in the current state is Ω_t, while the reference (undeformed) state is denoted Ω_0.

Due to homogenization, a point $\mathbf{x}$ corresponds to material points $\mathcal{P}^{\mathbf{I}}$ and $\mathcal{P}^{\mathbf{L}}$ from each phase. Their motion is given by:

$$\chi_{\alpha}(\mathbf{X},\mathrm{t}) : \left\{\Omega_0 \to \Omega_\mathrm{t} : \mathbf{X}\left(\mathcal{P}^{\alpha}\right) \mapsto \mathbf{x}\left(\mathcal{P}^{\alpha},\mathrm{t}\right)\right. . \tag{A.1}$$

This mapping is illustrated in Fig. 2. Differentiation with respect to time gives the phase velocity:

$$\mathbf{x}'_{\alpha} = \frac{\partial \chi_{\alpha}\left(\mathcal{P}^{\alpha},\mathrm{t}\right)}{\partial \mathrm{t}}, \tag{A.2}$$

while the barycentric velocity of the mixture is:

$$\dot{\mathbf{x}} = \frac{1}{\rho}\sum_{\alpha}\rho^{\alpha}\mathbf{x}'_{\alpha}, \tag{A.3}$$

where $\rho = \sum \rho^{\alpha}$ is the total density. The brine's mass-averaged velocity $\mathbf{x}'_{\mathbf{L}}$ follows as

$$\mathbf{x}'_{\mathbf{L}} = \frac{1}{\rho^{\mathrm{LR}}}\sum_{\beta}\rho^{\mathbf{L}\beta}\mathbf{x}'_{\mathbf{L}\beta} = \sum_{\beta}\mathrm{w}^{\mathbf{L}\beta}\mathbf{x}'_{\mathbf{L}\beta}. \tag{A.4}$$

The seepage velocity describing brine advection relative to the ice matrix is defined by:

$$\mathbf{w}_{\mathbf{LI}} = \mathbf{x}'_{\mathbf{L}} - \mathbf{x}'_{\mathbf{I}}. \tag{A.5}$$

Finally, the diffusion velocity of a component relative to the ice can be expressed as the difference between the component and brine seepage velocities:

$$\mathbf{d}_{\beta\mathbf{L}} = \mathbf{w}_{\beta\mathbf{I}} - \mathbf{w}_{\mathbf{LI}}. \tag{A.6}$$

A.2. Derivation of microscale field equations

The time-dependent diffusion term $\beta_1(\tau) = \frac{q+1}{q+\exp\left(-\frac{\tau_1}{\tau}\right)}\beta_2$ contains the time constant τ_1 and a parameter q which bounds β_1 within $[\beta_2, \frac{q+1}{q}\beta_2]$ for $q \geq 0$, as illustrated by

$$\lim_{\tau\to 0}\beta_1(\tau) = \frac{q+1}{q}\beta_2$$
$$\lim_{\tau\to\infty}\beta_1 = \beta_2.$$

Thus, β_2 denotes the equilibrium limit of β_1. The compression factor a scales the potential ω_L. Salinity is rendered dimensionless via $\sigma = \frac{K_F i}{-\Delta T_0}\mathrm{S}^{\mathrm{Bulk}}\mathrm{Macro}$, with $K_F = -1.853\ \frac{\mathrm{Kkg}}{\mathrm{mol}}$ (cryoscopic constant) and Van't Hoff factor $i = 2$ for NaCl. Given seawater's typical salinity $\mathrm{S}^{\mathrm{Bulk}}\mathrm{Macro} = 0.598\ \frac{\mathrm{mol}}{\mathrm{kg}}$ or 35 ppt, the resulting freezing point depression is −2.2 K. For thermodynamic consistency, the equality of mixed second-order derivatives of ω_{LG} must hold. Taking functional derivatives gives the evolution equations

$$\begin{aligned} a\tau_0\frac{\partial \mathrm{n}^{\mathbf{I}}_{\mathrm{Micro}}}{\partial\tau} &= -\frac{\delta\omega_{LG}}{\delta \mathrm{n}^{\mathbf{I}}_{\mathrm{Micro}}} = -\frac{\partial\omega_L}{\partial \mathrm{n}^{\mathbf{I}}_{\mathrm{Micro}}} + a^2L_c^2\frac{\partial^2 \mathrm{n}^{\mathbf{I}}_{\mathrm{Micro}}}{\partial L^2_{Micro}} \\ &= -a^4(\mathrm{n}^{\mathbf{I}}_{\mathrm{Micro}})^3 + \frac{3}{2}a^3(\mathrm{n}^{\mathbf{I}}_{\mathrm{Micro}})^2 - \left(\frac{1}{2} - \left(m - \frac{1}{2}\sigma\right)\right)a^2\mathrm{n}^{\mathbf{I}}_{\mathrm{Micro}} \\ &\quad + a^2L_c^2\frac{\partial^2 \mathrm{n}^{\mathbf{I}}_{\mathrm{Micro}}}{\partial L^2_{Micro}} \\ &= a^2\mathrm{n}^{\mathbf{I}}_{\mathrm{Micro}}\left(-a^2(\mathrm{n}^{\mathbf{I}}_{\mathrm{Micro}})^2 + \frac{3}{2}a\mathrm{n}^{\mathbf{I}}_{\mathrm{Micro}} - \frac{1}{2} + m - \frac{1}{2}\sigma\right) \\ &\quad + a^2L_c^2\frac{\partial^2 \mathrm{n}^{\mathbf{I}}_{\mathrm{Micro}}}{\partial L^2_{Micro}} \end{aligned} \tag{A.7}$$

$$\tau_0\frac{\partial\sigma}{\partial\tau} = -\frac{\partial^2}{\partial L^2_{Micro}}\left(-\frac{\delta\omega_{LG}}{\delta\sigma}\right) = \frac{\partial^2}{\partial L^2_{Micro}}\frac{\partial\omega_{LG}}{\partial\sigma} \tag{A.8}$$

$$= L_c^2\frac{\partial^2}{\partial L^2_{Micro}}\left(\frac{1}{4}a^2(\mathrm{n}^{\mathbf{I}}_{\mathrm{Micro}})^2 + \beta_1\sigma\right) \tag{A.9}$$

Using the roots $\mathrm{n}^{\mathbf{I}}_{\mathrm{Micro}}(\sigma) = \frac{1}{4a}\left(3 \pm \sqrt{1+16m-8\sigma}\right)$, Eq. (A.7) can be factorized as

$$\begin{aligned} a\tau_0\frac{\partial \mathrm{n}^{\mathbf{I}}_{\mathrm{Micro}}}{\partial\tau} &= -a^4\mathrm{n}^{\mathbf{I}}_{\mathrm{Micro}}\left(\mathrm{n}^{\mathbf{I}}_{\mathrm{Micro}} - \frac{1}{4a}\left(3 - \sqrt{1+16m-8\sigma}\right)\right) \\ &\quad \cdot \left(\mathrm{n}^{\mathbf{I}}_{\mathrm{Micro}} - \frac{1}{4a}\left(3 + \sqrt{1+16m-8\sigma}\right)\right) + a^2L_c^2\frac{\partial^2 \mathrm{n}^{\mathbf{I}}_{\mathrm{Micro}}}{\partial L^2_{Micro}} \end{aligned}$$

The largest root $\mathrm{n}^{\mathbf{I}}_{\mathrm{Micro}}(\sigma) = \frac{1}{4a}(3+\sqrt{1+16m-8\sigma})$ corresponds to the right minimum of the potential $\omega_L - \frac{\beta_1}{2}\sigma^2$. Setting $\mathrm{n}^{\mathbf{I}}_{\mathrm{Micro}}(\sigma = \sigma_{min}) = 1$ with $\sigma_{min} = 0$ leads to $a = \frac{1}{4}(3+\sqrt{1+16m})$, ensuring $0 \leq \mathrm{n}^{\mathbf{I}}_{\mathrm{Micro}} \leq 1$.

The salinity flux depends on the equilibrium parameter $\beta_2 = \lim_{\tau\to\infty}\beta_1(\tau)$. For steady-state conditions, Eq. (A.9) integrates to

$$0 = \frac{\partial}{\partial L_{Micro}}\left(\frac{1}{4}a^2(\mathrm{n}^{\mathbf{I}}_{\mathrm{Micro}})^2 + \beta_2\sigma\right) + C_1. \tag{A.10}$$

with $C_1 = 0$ when both $\frac{\partial \mathrm{n}^{\mathbf{I}}_{\mathrm{Micro}}}{\partial L_{Micro}}$ and $\frac{\partial \sigma}{\partial L_{Micro}}$ vanish. A second integration yields

$$\beta_2(\sigma - \sigma_{min}) = \frac{1}{4}a^2\left((\mathrm{n}^{\mathbf{I}}_{\mathrm{Micro}})^2_{max} - (\mathrm{n}^{\mathbf{I}}_{\mathrm{Micro}})^2\right), \tag{A.11}$$

and with $\mathrm{n}^{\mathbf{I}}_{\mathrm{Micro}}(\sigma = \sigma_{max}) = (\mathrm{n}^{\mathbf{I}}_{\mathrm{Micro}})_{min}$, it is possible to derive Eq. (A.12)

$$\beta_2(\sigma_{max} - \sigma_{min}) = \frac{1}{4}a^2\left((\mathrm{n}^{\mathbf{I}}_{\mathrm{Micro}})^2_{max} - (\mathrm{n}^{\mathbf{I}}_{\mathrm{Micro}})^2_{min}\right). \tag{A.12}$$

From the condition for the steady state

$$\mathrm{n}^{\mathbf{I}}_{\mathrm{Micro}}(\sigma = \sigma_{max}) = (\mathrm{n}^{\mathbf{I}}_{\mathrm{Micro}})_{min} = \frac{1}{2} = \frac{1}{4a}\left(3 - \sqrt{1 + 16m - 8\sigma_{max}}\right), \tag{A.13}$$

$\sigma_{max} = -1 + 2m - \frac{1}{2}a(a-3)$ is obtained. If $\mathrm{n}^{\mathbf{I}}_{\mathrm{Micro}}(\sigma_{min} = 0) = (\mathrm{n}^{\mathbf{I}}_{\mathrm{Micro}})_{max} = 1$ then the equation appears as given in Eq. (A.14) below

$$\beta_2\sigma_{max} = \frac{1}{4}a^2\left(1 - \left(\frac{1}{2}\right)^2\right) = \frac{3}{16}a^2, \tag{A.14}$$

with consideration of Eqs. (A.12) and (A.13), it becomes possible to determine β_2 as shown in Eq. (A.15)

$$\beta_2 = \frac{3a^2}{-16 + 32m - 8a(a-3)}. \tag{A.15}$$

A.3. Interfacial mass transfer approach

Local jumps across singular surfaces are responsible for the mass exchange between ice and water. Following [104], the mass jump across a singular surface Γ is given as

$$\rho^{\mathbf{L}}\mathbf{w}_{\mathbf{L}\Gamma} \cdot \mathbf{n}_\Gamma = \left(\rho^{\mathbf{L}+}\mathbf{w}^+_{\mathbf{L}\Gamma} - \rho^{\mathbf{L}-}\mathbf{w}^-_{\mathbf{L}\Gamma}\right) \cdot \mathbf{n}_\Gamma = 0, \tag{A.16}$$

In Eq. (A.16), + represents the direction of moving front. The normal vector $\mathbf{n}_\Gamma$ in outward-looking (+) direction represents ice and in inward-looking (−) direction represents water. This allows one to write

$$\begin{aligned} \mathbf{n}^+_\Gamma &= \mathbf{n}_\Gamma \quad \text{and} \quad \mathbf{n}^-_\Gamma = -\mathbf{n}_\Gamma \\ \rho^{\mathbf{L}+}\mathbf{w}^+_{\mathbf{L}\Gamma} &= \rho^{\mathbf{I}}\mathbf{w}_{\mathbf{I}\Gamma} \quad \text{and} \quad \rho^{\mathbf{L}-}\mathbf{w}^-_{\mathbf{L}\Gamma} = \rho^{\mathbf{L}}\mathbf{w}_{\mathbf{L}\Gamma}, \end{aligned} \tag{A.17}$$

Following Eq. (A.17), the mass jump can be written as

$$(\rho^{\mathbf{I}}\mathbf{w}_{\mathbf{I}\Gamma} - \rho^{\mathbf{L}}\mathbf{w}_{\mathbf{L}\Gamma}) \cdot \mathbf{n}_\Gamma = 0. \tag{A.18}$$

Based on Eq. (A.18), the interfacial mass transfer can then be written as

$$\hat{\rho}^{\mathbf{I}} = \rho^{\mathbf{I}}\mathbf{w}_{\mathbf{I}\Gamma} \cdot \mathbf{n}_\Gamma \quad \text{and} \quad \hat{\rho}^{\mathbf{L}} = -\rho^{\mathbf{L}}\mathbf{w}_{\mathbf{L}\Gamma} \cdot \mathbf{n}_\Gamma, \tag{A.19}$$

with the internal relation

$$\hat{\rho}^{\mathbf{I}} + \hat{\rho}^{\mathbf{L}} = 0. \tag{A.20}$$

Constrained by the internal relation (Eq. (A.20)), relation between the interfacial mass production (Eq. (A.19)) and continuum mass production can then be given as

$$\hat{\rho}^{\mathbf{I}}\mathrm{d}v \triangleq \hat{\rho}^{\mathbf{L}}_\Gamma \mathrm{d}a_\Gamma \quad \text{and} \quad \hat{\rho}^{\mathbf{L}}\mathrm{d}v \triangleq \hat{\rho}^{\mathbf{I}}_\Gamma \mathrm{d}a_\Gamma, \tag{A.21}$$

with $\mathrm{d}v$ being the unit volume of REV and $\mathrm{d}a_\Gamma$ representing the area of the interface, as given in Eq. (A.22)

$$\mathrm{d}a_\Gamma := \int_{A_{\mathrm{REV}}} \mathrm{d}a_{\Gamma\,\mathrm{REV}}. \tag{A.22}$$

The interfacial area can be written as the ratio of internal phase change with respect to overall volume

$$a_\Gamma := \frac{\mathrm{d}a_\Gamma}{\mathrm{d}v} \tag{A.23}$$

Therefore, Eq. (A.23) modifies the Eq. (A.21) as

$$\hat{\rho}^{\mathbf{I}} = a_\Gamma\hat{\rho}^{\mathbf{L}}_\Gamma \quad \text{and} \quad \hat{\rho}^{\mathbf{L}} = a_\Gamma\hat{\rho}^{\mathbf{I}}_\Gamma. \tag{A.24}$$

Data availability

Data will be made available on request.

References

[1] Martinson DG. Antarctic Sea Ice and Global Warming. In: Our warming planet. World Scientific; 2018, p. 309–27. http://dx.doi.org/10.1142/9789813148796_0015, URL http://www.worldscientific.com/doi/abs/10.1142/9789813148796_0015.

[2] Thomas DN, editor. Sea ice. 3rd ed.. Chichester, UK ; Hoboken, NJ: John Wiley & Sons; 2017.

[3] Stroeve JC, Serreze MC, Holland MM, Kay JE, Malanik J, Barrett AP. The Arctic's rapidly shrinking sea ice cover: a research synthesis. Clim Change 2012;110(3–4):1005–27. http://dx.doi.org/10.1007/s10584-011-0101-1, URL http://link.springer.com/10.1007/s10584-011-0101-1.

[4] Parkinson CL. A 40-y record reveals gradual Antarctic sea ice increases followed by decreases at rates far exceeding the rates seen in the Arctic. Proc Natl Acad Sci USA 2019;116(29):14414–23. http://dx.doi.org/10.1073/pnas.1906556116, URL https://pnas.org/doi/full/10.1073/pnas.1906556116.

[5] Gilbert E, Holmes C. 2023'S Antarctic sea ice extent is the lowest on record. Weather 2024;79(2):46–51. http://dx.doi.org/10.1002/wea.4518, URL https://rmets.onlinelibrary.wiley.com/doi/10.1002/wea.4518.

[6] Cai W, Jia F, Li S, Purich A, Wang G, Wu L, Gan B, Santoso A, Geng T, Ng B, Yang Y, Ferreira D, Meehl GA, McPhaden MJ. Antarctic shelf ocean warming and sea ice melt affected by projected El Niño changes. Nat Clim Chang 2023;13(3):235–9. http://dx.doi.org/10.1038/s41558-023-01610-x, URL https://www.nature.com/articles/s41558-023-01610-x.

[7] Chung E-S, Kim S-J, Timmermann A, Ha K-J, Lee S-K, Stuecker MF, Rodgers KB, Lee S-S, Huang L. Antarctic sea-ice expansion and Southern Ocean cooling linked to tropical variability. Nat Clim Chang 2022;12(5):461–8. http://dx.doi.org/10.1038/s41558-022-01339-z, URL https://www.nature.com/articles/s41558-022-01339-z.

[8] Boetius A, Anesio AM, Deming JW, Mikucki JA, Rapp JZ. Microbial ecology of the cryosphere: sea ice and glacial habitats. Nat Rev Microbiol 2015;13(11):677–90. http://dx.doi.org/10.1038/nrmicro3522, URL https://www.nature.com/articles/nrmicro3522.

[9] Skatulla S, Audh RR, Cook A, Hepworth E, Johnson S, Lupascu DC, MacHutchon K, Marquart R, Mielke T, Omatuku E, Paul F, Rampai T, Schröder J, Schwarz C, Vichi M. Physical and mechanical properties of winter first-year ice in the antarctic marginal ice zone along the good hope line. Cryosphere 2022;16(7):2899–925. http://dx.doi.org/10.5194/tc-16-2899-2022, URL https://tc.copernicus.org/articles/16/2899/2022/.

[10] Weeks W, Assur A. The mechanical properties of sea ice. U.S. Cold Regions Research and Engineering Laboratory Cold regions science and engineering; 1967.

[11] Vancoppenolle M, Fichefet T, Bitz CM. Modeling the salinity profile of undeformed Arctic sea ice. Geophys Res Lett 2006;33(21). http://dx.doi.org/10.1029/2006GL028342, 2006GL028342. URL https://agupubs.onlinelibrary.wiley.com/doi/10.1029/2006GL028342.

[12] Zienkiewicz OC, Taylor RL, Zhu JZ. The finite element method: its basis and fundamentals. 7th ed.. Amsterdam: Elsevier, Butterworth-Heinemann; 2013, OCLC: ocn852808496.

[13] Malmgren F. On the properties of sea ice. John Griegs Boktr. 1927;1a(5):1–67.

[14] Cox GFN, Weeks WF. Equations for Determining the Gas and Brine Volumes in Sea-Ice Samples. J Glaciol 1983;29(102):306–16. http://dx.doi.org/10.3189/S0022143000008364, URL https://www.cambridge.org/core/product/identifier/S0022143000008364/type/journal_article.

[15] Eicken H. Salinity profiles of Antarctic sea ice: Field data and model results. J Geophys Res 1992;97(C10):15545–57. http://dx.doi.org/10.1029/92JC01588, URL https://agupubs.onlinelibrary.wiley.com/doi/10.1029/92JC01588.

[16] Worster MG, Kerr RC. The transient behaviour of alloys solidified from below prior to the formation of chimneys. J Fluid Mech 1994;269:23–44. http://dx.doi.org/10.1017/S0022112094001473, URL https://www.cambridge.org/core/product/identifier/S0022112094001473/type/journal_article.

[17] Worster MG. The Dynamics of Mushy Layers. In: Davis SH, Huppert HE, Müller U, Worster MG, editors. Interactive dynamics of convection and solidification. Dordrecht: Springer Netherlands; 1992, p. 113–38. http://dx.doi.org/10.1007/978-94-011-2809-4_20, URL http://link.springer.com/index/10.1007/978-94-011-2809-4_20.

[18] Worster MG. Convection In MUShy Layers. Annu Rev Fluid Mech 1997;29(1):91–122. http://dx.doi.org/10.1146/annurev.fluid.29.1.91, URL https://www.annualreviews.org/doi/10.1146/annurev.fluid.29.1.91.

[19] Notz D, Worster MG. Desalination processes of sea ice revisited. J Geophys Res 2009;114(C5). http://dx.doi.org/10.1029/2008JC004885, 2008JC004885. URL https://agupubs.onlinelibrary.wiley.com/doi/10.1029/2008JC004885.

[20] Wang Q, Zhang Y, Chai F, Zhang YJ, Zampieri L. Development of a total variation diminishing (TVD) sea ice transport scheme and its application in an ocean (SCHISM v5.11) and sea ice (icepack v1.3.4) coupled model on unstructured grids. Geosci Model Dev 2024;17(18):7067–81. http://dx.doi.org/10.5194/gmd-17-7067-2024, URL https://gmd.copernicus.org/articles/17/7067/2024/.

[21] Äijälä C, Nie Y, Gutiérrez-Loza L, De Falco C, Lauvset SK, Cheng B, Bailey DA, Uotila P. Impacts of the CICE sea ice model and ERA atmosphere on an antarctic MetROMS ocean model, MetROMS-UHel-v1.0. Geosci Model Dev 2025;18(15):4823–53. http://dx.doi.org/10.5194/gmd-18-4823-2025, URL https://gmd.copernicus.org/articles/18/4823/2025/.

[22] Blockley E, Fiedler E, Ridley J, Roberts L, West A, Copsey D, Feltham D, Graham T, Livings D, Rousset C, Schroeder D, Vancoppenolle M. The sea ice component of GC5: coupling SI^3 to HadGEM3 using conductive fluxes. Geosci Model Dev 2024;17(17):6799–817. http://dx.doi.org/10.5194/gmd-17-6799-2024, URL https://gmd.copernicus.org/articles/17/6799/2024/.

[23] Hossain MA, Zhu P, Ma L. Analysis of weak solutions of a phase-field model for sea ice evolution. Alex Eng J 2023;70:641–9. http://dx.doi.org/10.1016/j.aej.2023.03.009, URL https://www.sciencedirect.com/science/article/pii/S1110016823001722.

[24] Xie X, Chen Y, Dai L, Xu L. Experimental and numerical study of seawater freezing coupled with ice growth dynamics and heat/mass transfer. Appl Therm Eng 2025;278:127329. http://dx.doi.org/10.1016/j.applthermaleng.2025.127329, URL https://www.sciencedirect.com/science/article/pii/S1359431125019210.

[25] Itkin P, Liston GE. Combining observational data and numerical models to obtain a seamless high temporal resolution seasonal cycle of snow and ice mass balance at the MOSAiC central observatory. EGUsphere 2024;2024:1–36. http://dx.doi.org/10.5194/egusphere-2024-3402, URL https://egusphere.copernicus.org/preprints/2024/egusphere-2024-3402/.

[26] Weiss J, Dansereau V. Linking scales in sea ice mechanics. Phil. Trans R. Soc A. 2017;375(2086):20150352. http://dx.doi.org/10.1098/rsta.2015.0352, URL https://royalsocietypublishing.org/doi/10.1098/rsta.2015.0352.

[27] Fu D, Liu B, Qi Y, Yu G, Huang H, Qu L. Multiscale variations in Arctic sea ice motion and links to atmospheric and oceanic conditions. Cryosphere 2021;15(8):3797–811. http://dx.doi.org/10.5194/tc-15-3797-2021, URL https://tc.copernicus.org/articles/15/3797/2021/.

[28] Deng Q, Stechmann SN, Chen N. Particle-continuum multiscale modeling of sea ice floes. Multiscale Model Simul 2024;22(1):230–55. http://dx.doi.org/10.1137/23M155904X, arXiv:https://doi.org/10.1137/23M155904X.

[29] Kulkarni S, Agarwal A. Arctic sea ice variability and its multiscale association with Indian summer monsoon rainfall at different time scales. J Hydrol 2025. http://dx.doi.org/10.1016/j.jhydrol.2025.132729.

[30] Wei L, Freris NM. Arctic sea ice prediction based on multi-scale graph modeling with conservation laws. J Geophys Res: Atmospheres 2025;130(1):e2024JD042136. http://dx.doi.org/10.1029/2024JD042136, e2024JD042136 2024JD042136. arXiv:https://agupubs.onlinelibrary.wiley.com/doi/pdf/10.1029/2024JD042136. URL https://agupubs.onlinelibrary.wiley.com/doi/abs/10.1029/2024JD042136.

[31] Zheng Q, Wang R, Han G, Li W, Wang X, Shao Q, Wu X, Cao L, Zhou G, Hu S. A spatiotemporal multiscale deep learning model for subseasonal prediction of Arctic Sea ice. IEEE Trans Geosci Remote Sens 2024;62:1–22. http://dx.doi.org/10.1109/TGRS.2024.3355238.

[32] Biot MA. General theory of three-dimensional consolidation. J Appl Phys 1941;12(2):155–64. http://dx.doi.org/10.1063/1.1712886.

[33] Biot MA, Willis DG. The Elastic Coefficients of the Theory of Consolidation. J Appl Mech 1957;24(4):594–601. http://dx.doi.org/10.1115/1.4011606.

[34] Green AE, Naghdi PM. On Basic Equations For Mixtures. Quart J Mech Appl Math 1969;22(4):427–38. http://dx.doi.org/10.1093/qjmam/22.4.427.

[35] Bowen RM. The thermochemistry of a reacting mixture of elastic materials with diffusion. Arch Ration Mech Anal 1969;34:97–127. http://dx.doi.org/10.1007/BF00247461.

[36] Passman S. Mixtures of granular materials. Internat J Engrg Sci 1977;15(2):117–29. http://dx.doi.org/10.1016/0020-7225(77)90027-1.

[37] Drumheller DS. The theoretical treatment of a porous solid using a mixture theory. Int J Solids Struct 1978;14(6):441–56. http://dx.doi.org/10.1016/0020-7683(78)90009-4.

[38] de Boer R. Highlights in the Historical Development of the Porous Media Theory: Toward a Consistent Macroscopic Theory. Appl Mech Rev 1996;49(4):201–62. http://dx.doi.org/10.1115/1.3101926, URL https://asmedigitalcollection.asme.org/appliedmechanicsreviews/article/49/4/201/401138/Highlights-in-the-Historical-Development-of-the.

[39] Ehlers W. Foundations of multiphasic and porous materials. In: Ehlers W, Bluhm J, editors. Porous media. Berlin, Heidelberg: Springer Berlin Heidelberg; 2002, p. 3–86. http://dx.doi.org/10.1007/978-3-662-04999-0_1, URL http://link.springer.com/10.1007/978-3-662-04999-0_1.

[40] Ehlers W, Bluhm J. Porous media: theory, experiments and numerical applications. Berlin: Springer; 2011, OCLC. 751579205.

[41] Mandl L, Mielke A, Seyedpour SM, Ricken T. Affine transformations accelerate the training of physics-informed neural networks of a one-dimensional consolidation problem. Sci Rep 2023;13(1):15566.

[42] Seyedpour S, Nafisi S, Nabati M, Pierce D, Reichenbach J, Ricken T. Magnetic resonance imaging–based biomechanical simulation of cartilage: A systematic review. J Mech Behav Biomed Mater 2022;126:104963. http://dx.doi.org/10.1016/j.jmbbm.2021.104963, URL https://www.sciencedirect.com/science/article/pii/S1751616121005932.

[43] Seyedpour SM. Simulation of contaminant transport in groundwater: from Pore-scale to Large-scale. Shaker Verlag; 2021.

[44] Hassanizadeh M, Gray WG. General conservation equations for multi-phase systems: 1. Averaging procedure. Adv Water Resour 1979;2:131–44. http://dx.doi.org/10.1016/0309-1708(79)90025-3.

[45] Hassanizadeh M, Gray WG. General conservation equations for multi-phase systems: 2. Mass, momenta, energy, and entropy equations. Adv Water Resour 1979;2:191–203. http://dx.doi.org/10.1016/0309-1708(79)90035-6.

[46] Lewis RW, Schrefler BA. The finite element method in the static and dynamic deformation and consolidation of porous media. Chinchester: John Wiley & Sons; 1999.

[47] de Boer R, Bluhm J. Phase Transitions in Gas- and Liquid-Saturated Porous Solids. Transp Porous Media 1999;34(1/3):249–67. http://dx.doi.org/10.1023/A:1006577828659, URL http://link.springer.com/10.1023/A:1006577828659.

[48] Ricken T, Bluhm J. Remodeling and growth of living tissue: a multiphase theory. Arch Appl Mech 2010;80(5):453–65. http://dx.doi.org/10.1007/s00419-009-0383-1, URL http://link.springer.com/10.1007/s00419-009-0383-1.

[49] Ricken T, Sindern A, Bluhm J, Widmann R, Denecke M, Gehrke T, Schmidt T. Concentration driven phase transitions in multiphase porous media with application to methane oxidation in landfill cover layers. Z Angew Math Mech 2014;94(7–8):609–22. http://dx.doi.org/10.1002/zamm.201200198, URL https://onlinelibrary.wiley.com/doi/10.1002/zamm.201200198.

[50] Ricken T, Thom A, Gehrke T, Denecke M, Widmann R, Schulte M, Schmidt TC. Biological Driven Phase Transitions in Fully or Partly Saturated Porous Media: A Multi-Component FEM Simulation Based on the Theory of Porous Media. In: Giovine P, Mariano PM, Mortara G, editors. In: Views on microstructures in granular materials, vol. 44, Cham: Springer International Publishing; 2020, p. 157–83. http://dx.doi.org/10.1007/978-3-030-49267-0_8, URL http://link.springer.com/10.1007/978-3-030-49267-0_8. Series Title. Advances in Mechanics and Mathematics.

[51] Seyedpour SM, Ricken T. Modeling of contaminant migration in groundwater: A continuum mechanical approach using in the theory of porous media. PAMM 2016;16(1):487–8.

[52] Bluhm J, Ricken T, Bloßfeld M. Ice Formation in Porous Media. In: Pfeiffer F, Wriggers P, Markert B, editors. In: Advances in extended and multifield theories for continua, vol. 59, Berlin, Heidelberg: Springer Berlin Heidelberg; 2011, p. 153–74. http://dx.doi.org/10.1007/978-3-642-22738-7_8, URL http://link.springer.com/10.1007/978-3-642-22738-7_8. Series Title. Lecture Notes in Applied and Computational Mechanics.

[53] Ricken T, Bluhm J. Modeling fluid saturated porous media under frost attack. GAMM-Mitt 2010;33(1):40–56. http://dx.doi.org/10.1002/gamm.201010004, URL https://onlinelibrary.wiley.com/doi/10.1002/gamm.201010004.

[54] Bluhm J, Ricken T, Bloßfeld WM. Freezing and thawing processes in porous media – Experiment and Simulation. Proc Appl Math Mech 2009;9(1):387–8. http://dx.doi.org/10.1002/pamm.200910167, URL https://onlinelibrary.wiley.com/doi/10.1002/pamm.200910167.

[55] Bluhm J, Bloßfeld W, Ricken T. Energetic effects during phase transition under freezing-thawing load in porous media – a continuum multiphase description and FE-simulation. Z Angew Math Mech 2014;94(7–8):586–608. http://dx.doi.org/10.1002/zamm.201200154, URL https://onlinelibrary.wiley.com/doi/10.1002/zamm.201200154.

[56] Thom A, Ricken T. In Silico Modeling of Coupled Physical-Biogeochemical (p-BGC) Processes in Antarctic Sea Ice. Proc Appl Math Mech 2021;20(1):e202000308. http://dx.doi.org/10.1002/pamm.202000308, URL https://onlinelibrary.wiley.com/doi/10.1002/pamm.202000308.

[57] Thom A, Ricken T. Towards a physical model of Antarctic sea ice microstructure including biogeochemical processes using the extended Theory of Porous Media. Proc Appl Math Mech 2019;19(1):e201900285. http://dx.doi.org/10.1002/pamm.201900285, URL https://onlinelibrary.wiley.com/doi/10.1002/pamm.201900285.

[58] Schwarz A, Bluhm J, Schröder J. Modeling of freezing processes of ice floes within the framework of the TPM. Acta Mech 2020;231(8):3099–121. http://dx.doi.org/10.1007/s00707-020-02686-8, URL https://link.springer.com/10.1007/s00707-020-02686-8.

[59] Schwarz A, Bluhm J, Schröder J. Investigations on modeling of freezing processes within the framework of the Theory of Porous Media. Proc Appl Math Mech 2021;20(1):e202000251. http://dx.doi.org/10.1002/pamm.202000251, URL https://onlinelibrary.wiley.com/doi/10.1002/pamm.202000251.

[60] Koßler M, Schwarz A, Bluhm J, Schröder J. A coupled finite element formulation for the modeling of freezing processes within the theory of porous media using a discontinuous approximation for the volume fraction ice. PAMM 2023;23(3):e202300074. http://dx.doi.org/10.1002/pamm.202300074, arXiv:https://onlinelibrary.wiley.com/doi/pdf/10.1002/pamm.202300074. URL https://onlinelibrary.wiley.com/doi/abs/10.1002/pamm.202300074.

[61] Pathak R, Seyedpour SM, Kutschan B, Thom A, Thoms S, Ricken T. Modeling freezing and BioGeoChemical processes in Antarctic sea ice. PAMM 2024;24(2):e202400047. http://dx.doi.org/10.1002/pamm.202400047, arXiv:https://onlinelibrary.wiley.com/doi/pdf/10.1002/pamm.202400047. URL https://onlinelibrary.wiley.com/doi/abs/10.1002/pamm.202400047.

[62] Pathak R, Seyedpour SM, Kutschan B, Thom A, Thoms S, Ricken T. Simulating sea ice freezing using a continuum mechanical multi-phase and multi-component homogenization framework. Cold Reg Sci & Technol 2025;239:104591. http://dx.doi.org/10.1016/j.coldregions.2025.104591, URL https://www.sciencedirect.com/science/article/pii/S0165232X25001740.

[63] Pathak R, Seyedpour SM, Kutschan B, Thoms S, Ricken T. A coupled multiscale description of seasonal physical–BioGeoChemical dynamics in southern ocean marginal ice zone. Environ Model Softw 2025;185:106270. http://dx.doi.org/10.1016/j.envsoft.2024.106270, URL https://www.sciencedirect.com/science/article/pii/S1364815224003311.

[64] Kobayashi R. A Numerical Approach to Three-Dimensional Dendritic Solidification. Exp Math 1994;3(1):59–81. http://dx.doi.org/10.1080/10586458.1994.10504577, URL http://www.tandfonline.com/doi/abs/10.1080/10586458.1994.10504577.

[65] Thoms S, Kutschan B, Morawetz K. Phase-field theory of brine entrapment in sea ice: Short-time frozen microstructures. 2014, arXiv:1405.0304.

[66] Kutschan B, Morawetz K, Gemming S. Modeling the morphogenesis of brine channels in sea ice. Phys Rev E 2010;81(3):036106. http://dx.doi.org/10.1103/PhysRevE.81.036106, URL https://link.aps.org/doi/10.1103/PhysRevE.81.036106.

[67] Morawetz K, Thoms S, Kutschan B. Formation of brine channels in sea ice. Eur Phys J E 2017;40(3):25. http://dx.doi.org/10.1140/epje/i2017-11512-x, URL http://link.springer.com/10.1140/epje/i2017-11512-x.

[68] Kutschan B, Morawetz K, Thoms S. Dynamical mechanism of antifreeze proteins to prevent ice growth. Phys Rev E 2014;90(2):022711. http://dx.doi.org/10.1103/PhysRevE.90.022711, URL https://link.aps.org/doi/10.1103/PhysRevE.90.022711.

[69] Liu X, Yuan H, Zhao Y, Zhang J, Song J, Gong M. Unveiling the dynamics of ice crystal growth and evolution in solidifying seawater. Desalination 2025;614:119207. http://dx.doi.org/10.1016/j.desal.2025.119207, URL https://www.sciencedirect.com/science/article/pii/S0011916425006836.

[70] Liu X, Yuan H, Zhao Y, Zhang J, Song J. Multi-physical field coupling simulation of three-dimensional crystal-liquid interfacial evolution in freezing desalination. Desalination 2025;615:119230. http://dx.doi.org/10.1016/j.desal.2025.119230, URL https://www.sciencedirect.com/science/article/pii/S0011916425007064.

[71] Xie X, Chen Y, Dai L, Xu L. Coupled multi-physics simulation and experimental study of dynamic seawater freezing under volumetric driving forces. Desalination 2025;611:118924. http://dx.doi.org/10.1016/j.desal.2025.118924, URL https://www.sciencedirect.com/science/article/pii/S0011916425003996.

[72] Moj L, Foppe M, Deike R, Ricken T. Micro-macro modelling of steel solidification: A continuum mechanical, bi-phasic, two-scale model including thermal driven phase transition. GAMM-Mitt 2017;40(2):125–37. http://dx.doi.org/10.1002/gamm.201720004, URL https://onlinelibrary.wiley.com/doi/10.1002/gamm.201720004.

[73] Ricken T, Sindern A, Bluhm J, Widmann R, Denecke M, Gehrke T, Schmidt T. Concentration driven phase transitions in multiphase porous media with application to methane oxidation in landfill cover layers. ZAMM - J Appl Math Mech / Z Angew Math Mech 2014;94(7–8):609–22. http://dx.doi.org/10.1002/zamm.201200198.

[74] Seyedpour SM, Henning C, Kirmizakis P, Herbrandt S, Ickstadt K, Doherty R, Ricken T. Uncertainty with varying subsurface permeabilities reduced using coupled random field and extended theory of porous media contaminant transport models. Water 2023;15(1). http://dx.doi.org/10.3390/w15010159, URL https://www.mdpi.com/2073-4441/15/1/159.

[75] Seyedpour SM, Thom A, Ricken T. Simulation of contaminant transport through the vadose zone: A continuum mechanical approach within the framework of the extended theory of porous media (eTPM). Water 2023;15(2). http://dx.doi.org/10.3390/w15020343, URL https://www.mdpi.com/2073-4441/15/2/343.

[76] Truesdell C. Thermodynamics of homogeneous processes. In: Rational thermodynamics. New York, NY: Springer New York; 1984, p. 59–81. http://dx.doi.org/10.1007/978-1-4612-5206-1_3.

[77] Hohenberg P, Krekhov A. An introduction to the Ginzburg–Landau theory of phase transitions and nonequilibrium patterns. Phys Rep 2015;572:1–42. http://dx.doi.org/10.1016/j.physrep.2015.01.001, An introduction to the Ginzburg–Landau theory of phase transitions and nonequilibrium patterns. URL https://www.sciencedirect.com/science/article/pii/S0370157315000514.

[78] Tikhonov AN. Systems of differential equations containing small parameters in the derivatives. Mat. Sb. 1952;31(3):575–86.

[79] Ager BH. Studies on the density of naturally and artificially formed fresh-water ice. J Glaciol 1962;4(32):207–14. http://dx.doi.org/10.3189/S0022143000027404.

[80] Petrenko VF, Whitworth RW. Physics of Ice. Oxford: Oxford University Press; 1999.

[81] Beaglehole D, Nason D. Transition layer on the surface on ice. Surf Sci 1980;96(1):357–63. http://dx.doi.org/10.1016/0039-6028(80)90313-1, URL https://www.sciencedirect.com/science/article/pii/0039602880903131.

[82] Hobbs PV. Ice Physics. Oxford, New York: Oxford University Press; 1974.

[83] Zhang D, Wang D. Energy-decreasing second order exponential time differencing Runge–Kutta methods for nonlocal Cahn–Hilliard equation. Appl Math Lett 2024;150:108974. http://dx.doi.org/10.1016/j.aml.2023.108974, URL https://www.sciencedirect.com/science/article/pii/S0893965923004068.

[84] Horntrop DJ, Katsoulakis MA, Vlachos DG. Spectral methods for mesoscopic models of pattern formation. J Comput Phys 2001;173(1):364–90. http://dx.doi.org/10.1006/jcph.2001.6883, URL https://www.sciencedirect.com/science/article/pii/S0021999101968834.

[85] Kutschan B, Thoms S, Thom A, Pathak R, Ricken T. Phase boundary dynamics for ice nucleation and growth processes in fresh and sea water. Phys D: Nonlinear Phenom 2025;481:134855. http://dx.doi.org/10.1016/j.physd.2025.134855, URL https://www.sciencedirect.com/science/article/pii/S016727892500332X.

[86] Niessner J, Hassanizadeh SM. A model for two-phase flow in porous media including fluid-fluid interfacial area. Water Resour Res 2008;44(8). http://dx.doi.org/10.1029/2007WR006721, 2007WR006721. URL https://agupubs.onlinelibrary.wiley.com/doi/10.1029/2007WR006721.

[87] Graf T. Multiphasic flow processes in deformable porous media under consideration of fluid phase transitions. 2008, http://dx.doi.org/10.18419/OPUS-287, URL http://elib.uni-stuttgart.de/handle/11682/304.

[88] Maus S, Schneebeli M, Wiegmann A. An X-ray micro-tomographic study of the pore space, permeability and percolation threshold of young sea ice. Cryosphere 2021;15(8):4047–72. http://dx.doi.org/10.5194/tc-15-4047-2021, URL https://tc.copernicus.org/articles/15/4047/2021/.

[89] Krembs C, Gradinger R, Spindler M. Implications of brine channel geometry and surface area for the interaction of sympagic organisms in Arctic sea ice. J Exp Mar Biol Ecol 2000;243(1):55–80. http://dx.doi.org/10.1016/S0022-0981(99)00111-2, URL https://www.sciencedirect.com/science/article/pii/S0022098199001112.

[90] Eicken H. Deriving modes and rates of ice growth in the Weddell sea from microstructural, salinity and stable-isotope data. In: Antarctic sea ice: physical processes, interactions and variability. American Geophysical Union (AGU); 1998, p. 89–122. http://dx.doi.org/10.1029/AR074p0089.

[91] Zhen Z, Song M, Cai B, Zhang X, Liu Z, Gao R. Experimental and modeling studies on the growth characteristics of ice layers at different temperatures and salinities. Int J Heat Fluid Flow 2025;115:109868. http://dx.doi.org/10.1016/j.ijheatfluidflow.2025.109868, URL https://www.sciencedirect.com/science/article/pii/S0142727X25001262.

[92] Toyoda T, Sakamoto K, Toyota T, Tsujino H, Urakawa LS, Kawakami Y, Yamagami A, Komatsu KK, Yamanaka G, Tanikawa T, Shimada R, Nakano H. Improvement of sea ice thermodynamics with variable sea ice salinity and melt pond parameterizations in an OGCM. Ocean Model 2024;187:102288. http://dx.doi.org/10.1016/j.ocemod.2023.102288, URL https://www.sciencedirect.com/science/article/pii/S1463500323001282.

[93] Korosov A, Ying Y, Ólason E. Tuning parameters of a sea ice model using machine learning. Geosci Model Dev 2025. http://dx.doi.org/10.5194/gmd-18-885-2025.

[94] Lin Y, Yang Q, Li X, Dong X, Luo H, Nie Y, Wang J, Wang Y, Min C. Ice-kNN-south: A lightweight machine learning model for Antarctic sea ice prediction. J Geophys Res: Mach Learn Comput 2025;2(1):e2024JH000433. http://dx.doi.org/10.1029/2024JH000433, e2024JH000433 2024JH000433. arXiv:https://agupubs.onlinelibrary.wiley.com/doi/pdf/10.1029/2024JH000433. URL https://agupubs.onlinelibrary.wiley.com/doi/abs/10.1029/2024JH000433.

[95] Maus S. Growth rate dependence of the permeability and percolation threshold of young sea ice.. Faraday Discuss 2025. URL https://api.semanticscholar.org/CorpusID:275284584.

[96] Stofa MM, Abdani SR, Moubark AM, Zainuri MAAM, Ibrahim AA, Kamari NAM, Zulkifley MA. Recent developments of artificial intelligence methods for sea ice concentration monitoring using high-resolution imaging datasets. Ecol Inform. 2025;87:103132. http://dx.doi.org/10.1016/j.ecoinf.2025.103132, URL https://www.sciencedirect.com/science/article/pii/S1574954125001414.

[97] Moos S, Vichi M, Fripiat F, Tison J-L, de Wit A, Rampai T. Developing digital image processing methods to quantify internal and interfacial convection in the Hele-Shaw cell, with applications to the laboratory ice2013ocean boundary layer. J Glaciol 2025;71:e86. http://dx.doi.org/10.1017/jog.2025.10066.

[98] Gu F, Kauker F, Yang Q, Han B, Fang Y, Liu C. Effects of freezing temperature parameterization on simulated sea-ice thickness validated by mosaic observations. Geophys Res Lett 2024;51(12):e2024GL108281. http://dx.doi.org/10.1029/2024GL108281, e2024GL108281 2024GL108281. arXiv:https://agupubs.onlinelibrary.wiley.com/doi/pdf/10.1029/2024GL108281. URL https://agupubs.onlinelibrary.wiley.com/doi/abs/10.1029/2024GL108281.

[99] Pathak R, Gupte A, Seyedpour S, Ricken T, Kutschan B, Thoms S. Towards multi-fidelity models of coupled multi-x processes in sea ice within the antarctic marginal ice zone. Eng Mater Struct Syst Methods more Sustain Futur 2025;355. http://dx.doi.org/10.1201/9781003488644-168.

[100] Edel L, Xie J, Korosov A, Brajard J, Bertino L. Reconstruction of arctic sea ice thickness (1992–2010) based on a hybrid machine learning and data assimilation approach. Cryosphere 2025;19(2):731–52. http://dx.doi.org/10.5194/tc-19-731-2025, URL https://tc.copernicus.org/articles/19/731/2025/.

[101] Ardyna M, Mundy CJ, Mayot N, Matthes LC, Oziel L, Horvat C, Leu E, Assmy P, Hill V, Matrai PA, Gale M, Melnikov IA, Arrigo KR. Under-ice phytoplankton blooms: Shedding light on the "invisible" part of arctic primary production. Front Mar Sci 2020;7. http://dx.doi.org/10.3389/fmars.2020.608032, URL https://www.frontiersin.org/journals/marine-science/articles/10.3389/fmars.2020.608032.

[102] Kraitzman N, Grattepanche J-D, Sanders R, Klapper I. A mathematical model of microbially-induced convection in sea ice. EGUsphere 2024;2024:1–25. http://dx.doi.org/10.5194/egusphere-2024-2696, URL https://egusphere.copernicus.org/preprints/2024/egusphere-2024-2696/.

[103] Babin M, Deming JW, Maréchal E, Rapp JZ, Rysgaard S, Vancoppenolle M. Life in the frozen ocean. Annu Rev Mar Sci 2025. http://dx.doi.org/10.1146/annurev-marine-032123-025316, URL https://www.annualreviews.org/content/journals/10.1146/annurev-marine-032123-025316.

[104] Ehlers W, Häberle K. Interfacial Mass Transfer During Gas–Liquid Phase Change in Deformable Porous Media with Heat Transfer. Transp Porous Media 2016;114(2):525–56. http://dx.doi.org/10.1007/s11242-016-0674-2, URL http://link.springer.com/10.1007/s11242-016-0674-2.